Measurement of the e^{+}e^{-}→K_{s}^{0}K^{±}π^{∓}π^{0} and K_{s}^{0}K^{±}π^{∓}η cross sections using initial-state radiation

J. P. Lees *et al.* (The BaBar Collaboration)

Measurement of the $e^+e^- \to K_s^0 K^\pm \pi^\mp \pi^0$ and $K_s^0 K^\pm \pi^\mp \eta$ cross sections using initial-state radiation

J. P. Lees, V. Poireau, and V. Tisserand
Laboratoire d'Annecy-le-Vieux de Physique des Particules (LAPP),
Université de Savoie, CNRS/IN2P3, F-74941 Annecy-Le-Vieux, France

E. Grauges
Universitat de Barcelona, Facultat de Fisica, Departament ECM, E-08028 Barcelona, Spain

A. Palano
INFN Sezione di Bari and Dipartimento di Fisica, Università di Bari, I-70126 Bari, Italy

G. Eigen
University of Bergen, Institute of Physics, N-5007 Bergen, Norway

D. N. Brown and Yu. G. Kolomensky
Lawrence Berkeley National Laboratory and University of California, Berkeley, California 94720, USA

M. Fritsch, H. Koch, and T. Schroeder
Ruhr Universität Bochum, Institut für Experimentalphysik 1, D-44780 Bochum, Germany

C. Hearty[ab], T. S. Mattison[b], J. A. McKenna[b], and R. Y. So[b]
Institute of Particle Physics[a]; University of British Columbia[b],
Vancouver, British Columbia, Canada V6T 1Z1

V. E. Blinov[abc], A. R. Buzykaev[a], V. P. Druzhinin[ab], V. B. Golubev[ab], E. A. Kravchenko[ab], P. A. Lukin[ab],
A. P. Onuchin[abc], S. I. Serednyakov[ab], Yu. I. Skovpen[ab], E. P. Solodov[ab], and K. Yu. Todyshev[ab]
Budker Institute of Nuclear Physics SB RAS, Novosibirsk 630090[a],
Novosibirsk State University, Novosibirsk 630090[b],
Novosibirsk State Technical University, Novosibirsk 630092[c], Russia

A. J. Lankford
University of California at Irvine, Irvine, California 92697, USA

J. W. Gary and O. Long
University of California at Riverside, Riverside, California 92521, USA

A. M. Eisner, W. S. Lockman, and W. Panduro Vazquez
University of California at Santa Cruz, Institute for Particle Physics, Santa Cruz, California 95064, USA

D. S. Chao, C. H. Cheng, B. Echenard, K. T. Flood, D. G. Hitlin, J. Kim,
T. S. Miyashita, P. Ongmongkolkul, F. C. Porter, and M. Röhrken
California Institute of Technology, Pasadena, California 91125, USA

Z. Huard, B. T. Meadows, B. G. Pushpawela, M. D. Sokoloff, and L. Sun*
University of Cincinnati, Cincinnati, Ohio 45221, USA

J. G. Smith and S. R. Wagner
University of Colorado, Boulder, Colorado 80309, USA

D. Bernard and M. Verderi
Laboratoire Leprince-Ringuet, Ecole Polytechnique, CNRS/IN2P3, F-91128 Palaiseau, France

D. Bettoni^a, C. Bozzi^a, R. Calabrese^{ab}, G. Cibinetto^{ab}, E. Fioravanti^{ab}, I. Garzia^{ab}, E. Luppi^{ab}, and V. Santoro^a

INFN Sezione di Ferrara^a; Dipartimento di Fisica e Scienze della Terra, Università di Ferrara^b, I-44122 Ferrara, Italy

A. Calcaterra, R. de Sangro, G. Finocchiaro, S. Martellotti,
P. Patteri, I. M. Peruzzi, M. Piccolo, M. Rotondo, and A. Zallo

INFN Laboratori Nazionali di Frascati, I-00044 Frascati, Italy

S. Passaggio and C. Patrignani†

INFN Sezione di Genova, I-16146 Genova, Italy

H. M. Lacker

Humboldt-Universität zu Berlin, Institut für Physik, D-12489 Berlin, Germany

B. Bhuyan

Indian Institute of Technology Guwahati, Guwahati, Assam, 781 039, India

U. Mallik

University of Iowa, Iowa City, Iowa 52242, USA

C. Chen, J. Cochran, and S. Prell

Iowa State University, Ames, Iowa 50011, USA

H. Ahmed

Physics Department, Jazan University, Jazan 22822, Kingdom of Saudi Arabia

A. V. Gritsan

Johns Hopkins University, Baltimore, Maryland 21218, USA

N. Arnaud, M. Davier, F. Le Diberder, A. M. Lutz, and G. Wormser

*Laboratoire de l'Accélérateur Linéaire, IN2P3/CNRS et Université Paris-Sud 11,
Centre Scientifique d'Orsay, F-91898 Orsay Cedex, France*

D. J. Lange and D. M. Wright

Lawrence Livermore National Laboratory, Livermore, California 94550, USA

J. P. Coleman, E. Gabathuler,‡ D. E. Hutchcroft, D. J. Payne, and C. Touramanis

University of Liverpool, Liverpool L69 7ZE, United Kingdom

A. J. Bevan, F. Di Lodovico, and R. Sacco

Queen Mary, University of London, London, E1 4NS, United Kingdom

G. Cowan

University of London, Royal Holloway and Bedford New College, Egham, Surrey TW20 0EX, United Kingdom

Sw. Banerjee, D. N. Brown, and C. L. Davis

University of Louisville, Louisville, Kentucky 40292, USA

A. G. Denig, W. Gradl, K. Griessinger, A. Hafner, and K. R. Schubert

Johannes Gutenberg-Universität Mainz, Institut für Kernphysik, D-55099 Mainz, Germany

R. J. Barlow§ and G. D. Lafferty

University of Manchester, Manchester M13 9PL, United Kingdom

R. Cenci, A. Jawahery, and D. A. Roberts

University of Maryland, College Park, Maryland 20742, USA

R. Cowan

Massachusetts Institute of Technology, Laboratory for Nuclear Science, Cambridge, Massachusetts 02139, USA

S. H. Robertson

Institute of Particle Physics and McGill University, Montréal, Québec, Canada H3A 2T8

B. Dey[a], N. Neri[a], and F. Palombo[ab]

INFN Sezione di Milano[a]; Dipartimento di Fisica, Università di Milano[b], I-20133 Milano, Italy

R. Cheaib, L. Cremaldi, R. Godang,[¶] and D. J. Summers

University of Mississippi, University, Mississippi 38677, USA

P. Taras

Université de Montréal, Physique des Particules, Montréal, Québec, Canada H3C 3J7

G. De Nardo and C. Sciacca

*INFN Sezione di Napoli and Dipartimento di Scienze Fisiche,
Università di Napoli Federico II, I-80126 Napoli, Italy*

G. Raven

NIKHEF, National Institute for Nuclear Physics and High Energy Physics, NL-1009 DB Amsterdam, The Netherlands

C. P. Jessop and J. M. LoSecco

University of Notre Dame, Notre Dame, Indiana 46556, USA

K. Honscheid and R. Kass

Ohio State University, Columbus, Ohio 43210, USA

A. Gaz[a], M. Margoni[ab], M. Posocco[a], G. Simi[ab], F. Simonetto[ab], and R. Stroili[ab]

INFN Sezione di Padova[a]; Dipartimento di Fisica, Università di Padova[b], I-35131 Padova, Italy

S. Akar, E. Ben-Haim, M. Bomben, G. R. Bonneaud, G. Calderini, J. Chauveau, G. Marchiori, and J. Ocariz

*Laboratoire de Physique Nucléaire et de Hautes Energies,
IN2P3/CNRS, Université Pierre et Marie Curie-Paris6,
Université Denis Diderot-Paris7, F-75252 Paris, France*

M. Biasini[ab], E. Manoni[a], and A. Rossi[a]

INFN Sezione di Perugia[a]; Dipartimento di Fisica, Università di Perugia[b], I-06123 Perugia, Italy

G. Batignani[ab], S. Bettarini[ab], M. Carpinelli[ab],[**] G. Casarosa[ab], M. Chrzaszcz[a], F. Forti[ab],
M. A. Giorgi[ab], A. Lusiani[ac], B. Oberhof[ab], E. Paoloni[ab], M. Rama[a], G. Rizzo[ab], and J. J. Walsh[a]

INFN Sezione di Pisa[a]; Dipartimento di Fisica, Università di Pisa[b]; Scuola Normale Superiore di Pisa[c], I-56127 Pisa, Italy

A. J. S. Smith

Princeton University, Princeton, New Jersey 08544, USA

F. Anulli[a], R. Faccini[ab], F. Ferrarotto[a], F. Ferroni[ab], A. Pilloni[ab], and G. Piredda[a‡]

*INFN Sezione di Roma[a]; Dipartimento di Fisica,
Università di Roma La Sapienza[b], I-00185 Roma, Italy*

C. Bünger, S. Dittrich, O. Grünberg, M. Heß, T. Leddig, C. Voß, and R. Waldi

Universität Rostock, D-18051 Rostock, Germany

T. Adye and F. F. Wilson

Rutherford Appleton Laboratory, Chilton, Didcot, Oxon, OX11 0QX, United Kingdom

S. Emery and G. Vasseur

CEA, Irfu, SPP, Centre de Saclay, F-91191 Gif-sur-Yvette, France

D. Aston, C. Cartaro, M. R. Convery, J. Dorfan, W. Dunwoodie, M. Ebert, R. C. Field, B. G. Fulsom,
M. T. Graham, C. Hast, W. R. Innes, P. Kim, D. W. G. S. Leith, S. Luitz, D. B. MacFarlane,

D. R. Muller, H. Neal, B. N. Ratcliff, A. Roodman, M. K. Sullivan, J. Va'vra, and W. J. Wisniewski

SLAC National Accelerator Laboratory, Stanford, California 94309 USA

M. V. Purohit and J. R. Wilson

University of South Carolina, Columbia, South Carolina 29208, USA

A. Randle-Conde and S. J. Sekula

Southern Methodist University, Dallas, Texas 75275, USA

M. Bellis, P. R. Burchat, and E. M. T. Puccio

Stanford University, Stanford, California 94305, USA

M. S. Alam and J. A. Ernst

State University of New York, Albany, New York 12222, USA

R. Gorodeisky, N. Guttman, D. R. Peimer, and A. Soffer

Tel Aviv University, School of Physics and Astronomy, Tel Aviv, 69978, Israel

S. M. Spanier

University of Tennessee, Knoxville, Tennessee 37996, USA

J. L. Ritchie and R. F. Schwitters

University of Texas at Austin, Austin, Texas 78712, USA

J. M. Izen and X. C. Lou

University of Texas at Dallas, Richardson, Texas 75083, USA

F. Bianchi[ab], F. De Mori[ab], A. Filippi[a], and D. Gamba[ab]

INFN Sezione di Torino[a]; Dipartimento di Fisica, Università di Torino[b], I-10125 Torino, Italy

L. Lanceri and L. Vitale

INFN Sezione di Trieste and Dipartimento di Fisica, Università di Trieste, I-34127 Trieste, Italy

F. Martinez-Vidal and A. Oyanguren

IFIC, Universitat de Valencia-CSIC, E-46071 Valencia, Spain

J. Albert[b], A. Beaulieu[b], F. U. Bernlochner[b], G. J. King[b], R. Kowalewski[b],
T. Lueck[b], I. M. Nugent[b], J. M. Roney[b], R. J. Sobie[ab], and N. Tasneem[b]

Institute of Particle Physics[a]; University of Victoria[b], Victoria, British Columbia, Canada V8W 3P6

T. J. Gershon, P. F. Harrison, and T. E. Latham

Department of Physics, University of Warwick, Coventry CV4 7AL, United Kingdom

R. Prepost and S. L. Wu

University of Wisconsin, Madison, Wisconsin 53706, USA

The processes $e^+e^- \rightarrow K_S^0 K^\pm \pi^\mp \pi^0$ and $e^+e^- \rightarrow K_S^0 K^\pm \pi^\mp \eta$ are studied over a continuum of energies from threshold to 4 GeV with the initial-state photon radiation method. Using 454 fb^{-1} of data collected with the *BABAR* detector at the SLAC PEP-II storage ring, the first measurements of the cross sections for these processes are obtained. The intermediate resonance structures from $K^{*0}(K\pi)^0$, $K^*(892)^\pm (K\pi)^\mp$ and $K_S^0 K^\pm \rho^\mp$ are studied. The J/ψ is observed in all of these channels, and corresponding branching fractions are measured.

PACS numbers: 13.66.Bc, 14.40.-n, 13.25.Jx

---

*Now at: Wuhan University, Wuhan 43072, China

†Now at: Università di Bologna and INFN Sezione di Bologna,

I. INTRODUCTION

Measurements of low-energy e^+e^- hadronic cross sections are important ingredients for the standard model prediction of the muon anomalous magnetic moment [1] and provide a wealth of spectroscopic information. At an e^+e^- collider, a continuous spectrum of collision energies below the nominal e^+e^- center-of-mass (c.m.) energy can be attained by selecting events with initial-state radiation (ISR), as proposed in Ref. [2] and discussed in Refs. [3–5].

At energies below a few GeV, individual exclusive final states must be studied in order to understand the experimental acceptance. The cross section $\sigma_{\gamma f}$ for an incoming e^+e^- pair colliding at a c.m. energy $\sqrt{s}$ to radiate a photon of energy E_γ and then annihilate into a specific final state f is related to the corresponding direct $e^+e^- \to f$ cross section σ_f by:

$$\frac{d\sigma_{\gamma f}(s,x)}{dx} = W(s,x)\sigma_f(E_{\text{c.m.}}) , \qquad (1)$$

where $x = 2E_\gamma/\sqrt{s}$ and $E_{\text{c.m.}} = \sqrt{s(1-x)}$ is the effective center-of-mass energy at which the state f is produced. The radiator function $W(s,x)$, or probability density for photon emission, can be evaluated to better than 1% accuracy [6].

Previously, we presented measurements of low-energy cross sections for many exclusive hadronic reactions using the ISR method, including a number of final states with two kaons in the final state, such as $f = K^+K^-$ [7], $K^+K^-\pi^+\pi^-$ [8], $K_S^0 K_L^0$, $K_S^0 K_L^0 \pi^+\pi^-$, $K_S^0 K_S^0 \pi^+\pi^-$ and $K_S^0 K_S^0 K^+K^-$ [9], $K_S^0 K^\pm\pi^\mp$ [10], $K_S^0 K_L^0 \pi^0$ and $K_S^0 K_L^0 \pi^0\pi^0$ [11]. Here, we extend our program and report measurements of the $e^+e^- \to K_S^0 K^\pm\pi^\mp\pi^0$ and $K_S^0 K^\pm\pi^\mp\eta$ channels, including studies of the intermediate resonant substructure.

II. THE BABAR DETECTOR AND DATA SET

The results presented in this analysis are based on a sample of e^+e^- annihilation data collected at $E_{\text{c.m.}} = 10.58$ GeV with the BABAR detector [12] at the SLAC PEP-II storage ring, and correspond to an integrated luminosity of 454 fb^{-1} [13].

Charged-particle momenta are measured in a tracking system consisting of a five-layer double-sided silicon vertex tracker (SVT) and a 40-layer central drift chamber (DCH), immersed in a 1.5 T axial magnetic field. An internally reflecting ring-imaging Cherenkov detector (DIRC) with fused silica radiators provides charged-particle identification (PID). A CsI electromagnetic calorimeter (EMC) is used to detect and identify photons and electrons. Muons are identified in the instrumented magnetic flux-return system.

Charged pion and kaon candidates are selected using a likelihood function based on the specific ionization in the DCH and SVT, and the Cherenkov angle measured in the DIRC. Photon candidates are defined as clusters in the EMC that have a shape consistent with an electromagnetic shower and no associated charged track.

To study the signal efficiency as well as backgrounds from other ISR processes, a special package of Monte Carlo (MC) simulation programs for radiative processes has been developed. Algorithms for generating hadronic final states via ISR are derived from Ref. [14]. Multiple soft-photon emission from initial-state charged particles is implemented by means of the structure-function technique [15, 16], while extra photon radiation from final-state particles is simulated with the PHOTOS [17] package.

Large samples of signal $e^+e^- \to K_S^0 K^\pm\pi^\mp\pi^0\gamma$ and $K_S^0 K^\pm\pi^\mp\eta\gamma$ events are generated with this program, as well as samples of events from the principal ISR background sources, $e^+e^- \to K_S^0 K^\pm\pi^\mp\gamma$ and $e^+e^- \to K_S^0 K^\pm\pi^\mp\pi^0\pi^0\gamma$. The $K_S^0 K^\pm\pi^\mp\gamma$ generator is tuned to reproduce our measured [10] $E_{\text{c.m.}}$ dependence and resonant substructure. The other modes use smooth $E_{\text{c.m.}}$ dependences and phase space for the final state hadrons. The signal and $K_S^0 K^\pm\pi^\mp$ generators reproduce the kaon and pion kinematic distributions observed in the data, and we study the effect of resonances on the efficiency in each case below. In addition to the ISR sources, background arises from the non-ISR processes $e^+e^- \to q\bar{q}$ and $\tau^+\tau^-$. These events are simulated with the JETSET [18] and KORALB [19] event generators, respectively. All simulated events are processed through a detector simulation based on the GEANT4 [20] package and are analyzed in the same manner as the data.

III. EVENT SELECTION AND KINEMATICS

We require events to contain at least three photon candidates and at least four charged tracks, including at least one $K_S^0 \to \pi^+\pi^-$ candidate.

Photon candidates must lie within the acceptance of the EMC, defined by $0.35 < \theta < 2.4$ radians, where θ is the polar angle relative to the e^- beam direction. The photon candidate with highest energy is assumed to be the ISR photon, and is required to have energy $E^* > 3$ GeV, where the asterisk indicates a quantity evaluated in the e^+e^- c.m. frame. To reduce background from machine-induced soft photons, at least one additional photon candidate must have $E^* > 100$ MeV and another $E^* > 60$ MeV. We calculate the invariant mass

I-47921 Rimini, Italy
‡Deceased
§Now at: University of Huddersfield, Huddersfield HD1 3DH, UK
¶Now at: University of South Alabama, Mobile, Alabama 36688, USA
**Also at: Università di Sassari, I-07100 Sassari, Italy

$m_{\gamma\gamma}$ of each pair of photon candidates, and consider a pair to be a π^0 candidate if $0.09 < m_{\gamma\gamma} < 0.18$ GeV/c^2 and an η candidate if $0.47 < m_{\gamma\gamma} < 0.62$ GeV/c^2. Events with at least one π^0 or η candidate are retained.

We require at least two charged tracks in an event, of opposite charge, one identified as a kaon and one as a pion, that appear in the polar angle range $0.45 < \theta < 2.40$ radians. Each track must extrapolate to within 0.25 cm of the nominal e^+e^- collision point in the plane perpendicular to the beam axis and to within 3 cm along the axis.

The K_S^0 candidates are reconstructed in the $\pi^+\pi^-$ decay mode from pairs of oppositely charged tracks not identified as electrons. They must have an invariant mass within 15 MeV/c^2 of the nominal K_S^0 mass, and a well reconstructed vertex at least 2 mm away from the beam axis. The angle $\theta_{K_S^0}$ between their reconstructed total momentum and the line joining their vertex with the primary vertex position must satisfy $\cos(\theta_{K_S^0}) > 0.99$.

Each of these events is subjected to a set of 5-constraint (5C) kinematic fits, in which the four-momentum of the $K_S^0 K^\pm \pi^\mp \gamma_{ISR} \gamma\gamma$ system is required to equal that of the initial e^+e^- system and the invariant mass of the two non-ISR photon candidates is constrained to the nominal π^0 or η mass. The fits employ the full covariance matrices and provide χ^2 values and improved determinations of the particle momenta and angles, which are used in the subsequent analysis. Fits are performed for every π^0 and η candidate in the event, and we retain the combinations giving the lowest values of $\chi^2_{K_S^0 K^\pm \pi^\mp \pi^0}$ and $\chi^2_{K_S^0 K^\pm \pi^\mp \eta}$.
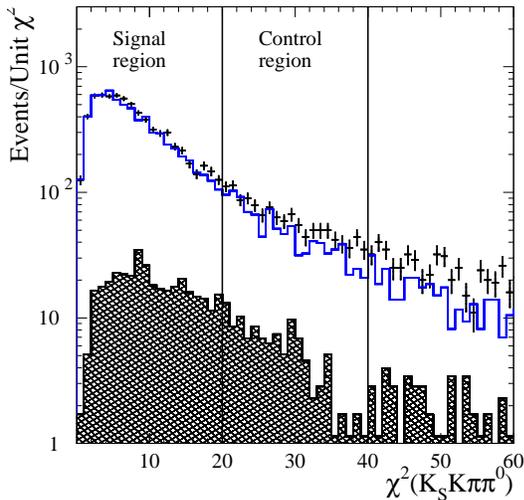

FIG. 1: Distribution of χ^2 from the 5-constraint fit for $K_S^0 K^\pm \pi^\mp \pi^0 \gamma$ candidates in the data (points). The open and cross-hatched histograms are the distributions for simulated signal and $q\bar{q}$ background events, respectively, normalized as described in the text. The signal and control regions are indicated.

IV. THE $K_S^0 K^\pm \pi^\mp \pi^0$ FINAL STATE

A. Event selection

The $\chi^2_{K_S^0 K^\pm \pi^\mp \pi^0}$ distribution for the selected $e^+e^- \to K_S^0 K^\pm \pi^\mp \pi^0 \gamma$ events is shown in Fig. 1, after subtraction of the small background from $q\bar{q}$ events, which is discussed below and shown in the figure as the cross-hatched histogram. The corresponding distribution for simulated, selected signal events is shown as the open histogram. It is normalized to the data integrated over the first five bins, where the lowest ISR background contributions are expected. These distributions are broader than a typical 5C χ^2 distribution because of multiple soft-photon emission from the initial state, which is not taken into account in the fit but is present in both the data and simulation. Previous studies have found these effect to be well simulated, and we assign a systematic uncertainty in Section IV B. The remaining differences can be explained by ISR backgrounds, which we discuss in this subsection.

Signal event candidates are selected by requiring $\chi^2_{K_S^0 K^\pm \pi^\mp \pi^0} < 20$. Events with $20 < \chi^2_{K_S^0 K^\pm \pi^\mp \pi^0} < 40$ are used as a control sample to evaluate background. The signal and control samples contain 6859 (5656) and 1257(870) experimental (simulation) events, respectively.
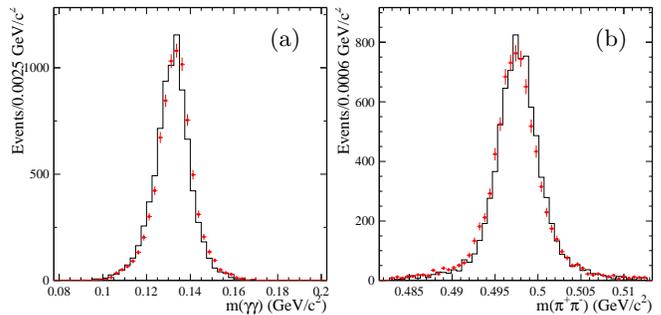

FIG. 2: The (a) $\gamma\gamma$ and (b) $\pi^+\pi^-$ invariant-mass distributions of the π^0 and K_S^0 candidates, respectively, in $K_S^0 K^\pm \pi^\mp \pi^0$ events in the $\chi^2_{K_S^0 K^\pm \pi^\mp \pi^0}$ signal region, for the selected data (points) and the signal simulation (histograms).

Figure 2(a) compares the $\gamma\gamma$ invariant-mass distribution of the π^0 candidate for data events in the signal region with the prediction of the signal-event simulation. The π^0 peak in the simulation is shifted with respect to the data by -0.6 ± 0.2 MeV/c^2, while the standard deviations are consistent with each other ($\sigma_{\text{DATA}} = 6.65\pm0.14$ MeV/c^2 and $\sigma_{\text{MC}} = 6.70 \pm 0.12$ MeV/c^2).

The corresponding distributions of the $\pi^+\pi^-$ invariant mass of the K_S^0 candidate are shown in Fig. 2(b). In this case, a shift in the peak values of 0.23 ± 0.05 MeV/c^2 is observed between data and simulation. The widths are found to be somewhat different: $\sigma_{DATA} = 2.40 \pm 0.03$ MeV/c^2 and $\sigma_{MC} = 2.30\pm0.03$ MeV/c^2. Our selec-

tion criteria on the π^0 and K_S^0 masses are unrestrictive enough to ensure the shifts do not affect the result.

The distribution of the invariant mass of the final-state hadronic system for all data events in the signal region is shown as the open histogram in Fig. 3. A narrow peak due to $J/\psi \to K_S^0 K^\pm \pi^\mp \pi^0$ decays is clearly visible.
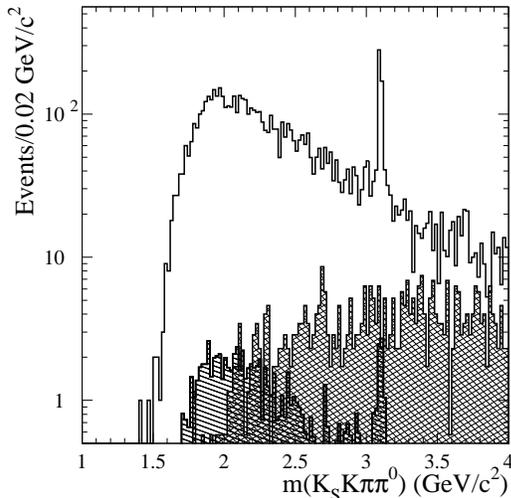

FIG. 3: Distribution of the fitted $K_S^0 K^\pm \pi^\mp \pi^0$ invariant mass for data events in the $K_S^0 K^\pm \pi^\mp \pi^0$ signal region. The hatched and cross-hatched distributions show the estimated backgrounds evaluated from ISR and $q\bar{q}$ events, respectively.

Cross sections for backgrounds from $q\bar{q}$ processes are poorly known. In simulation, the dominant such process is $e^+ e^- \to K_S^0 K^\pm \pi^\mp \pi^0 \pi^0$, in which an energetic photon from one of the π^0 decays is erroneously taken as the ISR photon. These events have kinematic properties similar to signal events and yield a χ^2 distribution peaked at low values. This component can be evaluated from the data, since such events produce a peak at the π^0 invariant mass when the photon erroneously identified as the ISR photon is combined with another photon in the event. Following the procedure described in Ref. [10], we use the MC mass distribution, and normalize it to the data in the region $2 < m < 4$ GeV, where the π^0 peak is prominent. A consistent normalization factor is obtained from the 4–6 GeV/c^2 region. For lower masses, we see no significant π^0 peak in the data, and we use the very small MC prediction with the same normalization. The normalized contribution of the $q\bar{q}$ background to the distributions of Figs. 1 and 3 is shown by the cross-hatched histograms. For subsequent distributions, the $q\bar{q}$ background is subtracted.

The remaining background arises from ISR processes, dominated by $e^+ e^- \to K_S^0 K^\pm \pi^\mp \gamma$ events combined with random photons, and by $e^+ e^- \to K_S^0 K^\pm \pi^\mp \pi^0 \pi^0 \gamma$ events. These have broad distributions in χ^2, and can be estimated from the control region of the χ^2 distribution. The points with errors in Fig. 4 show the difference between the data and the normalized simulated $\chi^2_{K_S^0 K^\pm \pi^\mp \pi^0}$ dis-

tributions of Fig. 1. Assuming good signal simulation and low ISR background at low χ^2, this gives an estimate of the shape of the distribution for the total remaining background. The simulation of the ISR $K_S^0 K^\pm \pi^\mp$ background shows a consistent shape and, when normalized to our previous measurement [10], accounts for about 10% of the entries. The simulated ISR $K_S^0 K^\pm \pi^\mp \pi^0 \pi^0$ background also has a consistent shape, and is expected to be much larger. Normalizing to a cross section nine times larger and adding the ISR $K_S^0 K^\pm \pi^\mp$ prediction, we obtain the simulated distribution shown as the histogram in Fig. 4. This demonstrates sufficient understanding of the shape of the background distribution, and we assume that all remaining background has the simulated shape. The genuine signal and the ISR background in
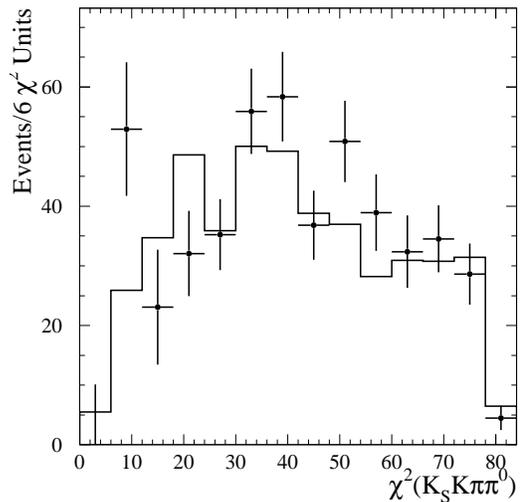

FIG. 4: The $\chi^2_{K_S^0 K^\pm \pi^\mp \pi^0}$ distributions of the ISR background determined from the data (points with errors) and the sum of MC simulations for the processes $e^+ e^- \to K_S^0 K^\pm \pi^\mp \gamma$ and $e^+ e^- \to K_S^0 K^\pm \pi^\mp \pi^0 \pi^0 \gamma$ (open histogram) described in the text.

any distribution other than the χ^2 are estimated bin-by-bin using the numbers of selected events in that bin in the signal and control regions, N_1 and N_2, after subtraction of the respective $q\bar{q}$ backgrounds. We take N_1 (N_2) to be the sum of the numbers of genuine signal N_{1S} (N_{2S}) and ISR background events N_{1B} (N_{2B}) in the signal (control) region. From the signal simulation, we obtain $N_{1S}/N_{2S} = \alpha = 6.59 \pm 0.24$, and from the ISR background simulation $N_{1B}/N_{2B} = \beta = 0.49 \pm 0.07$. The observed values of N_1 and N_2 are 6509 ± 81 and 1146 ± 34, respectively. We then solve for

$$N_{1S} = \alpha \cdot \frac{N_1 - \beta \cdot N_2}{\alpha - \beta}, \qquad (2)$$

and N_{1B} in that bin.

The ISR background evaluated in this manner is shown by the hatched histogram in Fig. 3.

We find $N_{1S} = 6430 \pm 90$, where the uncertainty is

statistical. The systematic uncertainty in the $q\bar{q}$ background estimate is taken to be 50%, to account for the limited knowledge of the $q\bar{q}$ cross section. The systematic uncertainty in the ISR background estimate is, more conservatively, taken to be 100%. The total systematic uncertainty is evaluated in three regions of $E_{\mathrm{c.m.}}$. This yields relative uncertainties in N_{1S} of 2.5% for $E_{\mathrm{c.m.}} < 2$ GeV, 6.25% for $2 < E_{\mathrm{c.m.}} < 3$ GeV, and 10% for $E_{\mathrm{c.m.}} > 3$ GeV.

B. Detection efficiency

The reconstruction and selection efficiency for signal events is determined from the signal simulation, corrected for known differences with respect to data. The efficiencies for charged-track, photon, and K_S^0 reconstruction depend on the momentum and polar angle of the particle. The distributions of these variables are well described by the simulation for all relevant particles. The total event detection efficiency from the simulation, including the $K_S^0 \to \pi^+ \pi^-$ branching fraction of 0.692 [21] is shown as a function of $E_{\mathrm{c.m.}}$ in Fig. 5. A smooth parametrization, shown by the solid line, is used.

The π^0 detection efficiency was studied in our previous analysis [22] of $e^+e^- \to \omega\gamma \to \pi^+\pi^-\pi^0\gamma$ events, yielding corrections to the simulation as a function of the π^0 momentum and polar angle. Applying these event-by-event to the signal simulation yields an overall correction of $+2\pm1\%$, independent of $E_{\mathrm{c.m.}}$. Similarly, we incorporate corrections to the charged-track and K_S^0 reconstruction efficiencies making use of the results found in our previous studies of $e^+e^- \to \pi^+\pi^-\pi^+\pi^-\gamma$ [23] and $e^+e^- \to K_S^0 K_L^0\gamma$ [9] events, respectively, where the latter corrections also depend on the flight length of the K_S^0 meson transverse to the beam direction. Corrections of $+0.8\pm1.0\%$ for each of the $\pi^\pm$ and $K^\pm$, and $+1.1\pm1.0\%$ for the K_S^0, are derived, again independent of $E_{\mathrm{c.m.}}$. Similar corrections to the pion and kaon identification efficiencies amount to $0\pm2\%$.

We study a possible data-MC difference in the shape of the χ^2 distribution using the J/ψ signal, which has negligible non-ISR background. The increase in the J/ψ yield when loosening the χ^2 requirement from 20 to 200 is consistent with the expectation from simulation, and we estimate a correction of $+3.7 \pm 4.6\%$.

As a cross-check, using a fast simulation of the detector response for computational simplicity, we compare the results obtained for signal events generated with a phase-space model to those obtained for signal events generated with intermediate $K_S^0\pi^\mp$ resonances, specifically $e^+e^- \to K^*(892)^\pm K_S^0\pi^\mp$ and $K^{*0}K^\pm\pi^\mp$. No difference in efficiency larger than 0.5% is seen, and we assign a systematic uncertainty of 0.5% to account both for possible model dependence and for the choice of parametrization of the efficiency as a function of $E_{\mathrm{c.m.}}$. These corrections and uncertainties are listed in Table I. The total correction is $+8.6\%$
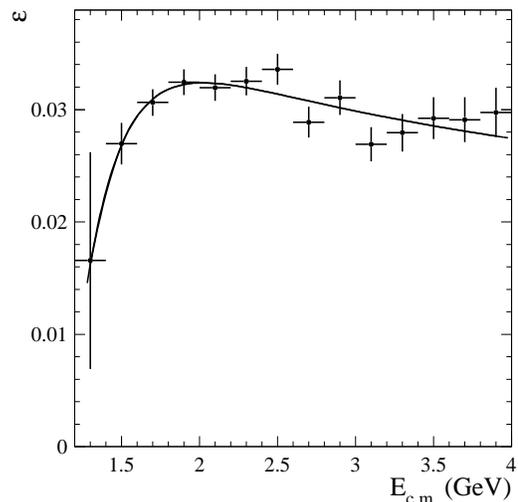

FIG. 5: Detection efficiency for $e^+e^- \to K_S^0 K^\pm\pi^\mp\pi^0$ events as a function of the hadronic invariant mass $E_{\mathrm{c.m.}} = m(K_S^0 K^\pm\pi^\mp\pi^0)$. The solid curve shows a fitted parametrization.

C. The cross section for $e^+e^- \to K_S^0 K^\pm\pi^\mp\pi^0$

The $e^+e^- \to K_S^0 K^\pm\pi^\mp\pi^0$ cross section is obtained from:

$$\sigma(E_{\mathrm{c.m.}}) = \frac{dN_{K_S^0 K^\pm\pi^\mp\pi^0}(E_{\mathrm{c.m.}})}{d\mathcal{L}(E_{\mathrm{c.m.}})\varepsilon(E_{\mathrm{c.m.}})R(E_{\mathrm{c.m.}})}, \qquad (3)$$

where $E_{\mathrm{c.m.}}$ is the invariant mass of the $K_S^0 K^\pm\pi^\mp\pi^0$ system, $dN_{K_S^0 K^\pm\pi^\mp\pi^0}$ is the number of signal $K_S^0 K^\pm\pi^\mp\pi^0$ events in the interval $dE_{\mathrm{c.m.}}$, $d\mathcal{L}(E_{\mathrm{c.m.}})$ is the differential luminosity, $\varepsilon(E_{\mathrm{c.m.}})$ is the corrected efficiency discussed in Section IV B, and $R(E_{\mathrm{c.m.}})$ is the correction to account for additional soft radiative photon emission from the initial state.

The differential luminosity $d\mathcal{L}(m)$ is calculated using the total PEP-II integrated luminosity $\mathcal{L} = 454\,\mathrm{fb}^{-1}$ and the probability density function for ISR photon emission. To first order it can be written as:

$$\frac{d\mathcal{L}}{dm} = \frac{\alpha}{\pi x}\left((2 - 2x + x^2)\log\frac{1+C}{1-C} - x^2 C\right)\frac{2m}{s}\mathcal{L}. \quad (4)$$

Here $m = m(K_S^0 K^\pm\pi^\mp\pi^0)$, $x = 1 - m^2/s$, $C = \cos\theta_0^*$, and θ_0^* defines the acceptance of the analysis in the polar angle of the ISR photon in the e^+e^- c.m. frame, $\theta_0^* < \theta_\gamma^* < 180^o - \theta_0^*$. Here, $\theta_0^* = 20^o$.

The radiative correction $R(E_{\mathrm{c.m.}})$ is determined using generator-level MC (without simulation of the detector response) as the ratio of the $K_S^0 K^\pm\pi^\mp\pi^0$ spectrum with soft photon emission to that at the Born level. We determine $R = 1.0029 \pm 0.0065$, independent of $E_{\mathrm{c.m.}}$. The combined systematic uncertainty in the luminosity and radiative correction is estimated to be 1.4%.

The fully corrected $e^+e^- \to K_S^0 K^\pm\pi^\mp\pi^0$ cross section is shown in Fig. 6 and listed in Table II, with statistical

uncertainties. The relative systematic uncertainties are summarized in Table I; their total ranges from 6.2% for $E_{\text{c.m.}} < 2$ GeV to 11.6% for $E_{\text{c.m.}} > 3$ GeV.

TABLE I: Summary of the corrections to, and systematic uncertainties in the $e^+e^- \to K_S^0 K^\pm \pi^\mp \pi^0$ cross section.

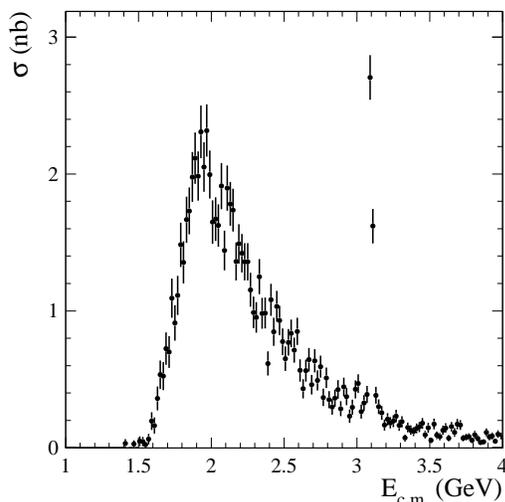| Source	Correction (%)	Systematic uncertainty (%)
π^0 reconstruction	+2.0	1.0
$K^\pm$, $\pi^\pm$ reconstruction	+1.6	2.0
K_S^0 reconstruction	+1.1	1.0
PID efficiency	0.0	2.0
χ^2 selection	+3.7	4.6
Background subtraction	—	2.5, < 2.0 GeV
		4.2, 2.0-3.0 GeV
		10.0, > 3.0 GeV
Model acceptance	—	0.5
Luminosity and Rad.Corr.	—	1.4
Total	+8.6	6.3, < 2.0 GeV
		7.1, 2.0-3.0 GeV
		11.5, > 3.0 GeV

FIG. 6: Cross section for the process $e^+e^- \to K_S^0 K^\pm \pi^\mp \pi^0$. The uncertainties are statistical.

D. Substructure in the $K_S^0 K^\pm \pi^\mp \pi^0$ final state

Previously, we studied single $K^*(892)$ production in the processes $e^+e^- \to K_S^0 K^\pm \pi^\mp$ and $K^+K^-\pi^0$ [10], and double $K^*(892)$ production, as well as ϕ, ρ, and f_0 production, in $e^+e^- \to K^+K^-\pi^+\pi^-$, $K^+K^-\pi^0\pi^0$ [8] and $K_S^0 K_L^0 \pi^+\pi^-$ [9]. Here, we expect single $K^*(892)$, double $K^*(892)$, ρ, and possibly other resonance contributions, but the statistical precision of the data sample is insufficient for competitive measurements of such processes. Since it is important to confirm, as far as possible, resonant cross sections measured in different final states, and

to verify expected isospin relations, we perform a simple study of those resonant subprocesses accessible with our data.
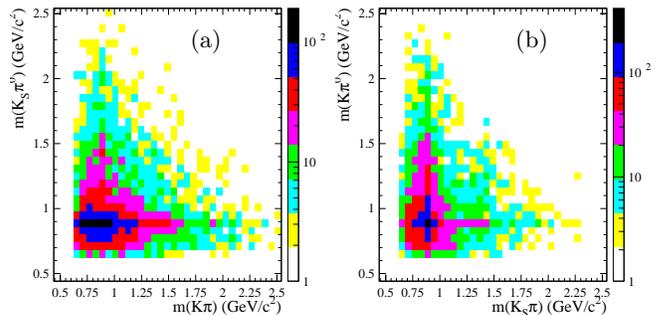

FIG. 7: Scatter plots of (a) the $K_S^0\pi^0$ vs. $K^\pm\pi^\mp$ and (b) $K^\pm\pi^0$ vs. $K_S^0\pi^\mp$ invariant masses in $e^+e^- \to K_S^0 K^\pm\pi^\mp\pi^0$ events.

Decays of the J/ψ are discussed below (Sec. VI), and for the study presented in this section we exclude the region $3.0 < E_{\text{c.m.}} < 3.2$ GeV. Figure 7(a) shows a scatter plot of the $K_S^0\pi^0$ vs. $K^\pm\pi^\mp$ invariant masses in the selected data sample, corrected for backgrounds as described above, while Fig. 7(b) shows the $K^\pm\pi^0$ vs. $K_S^0 \pi^\mp$ masses. Clear signals for charged and neutral $K^*(892)^0$ states are seen. Figure 8(a) is the projection of Fig. 7(a) onto the vertical axis, and shows a large $K^*(892)^0$ peak as well as possible structure near 1.43 GeV/c^2. This could arise from the $K_2^*(1430)$ or $K_0^*(1430)$ resonances, or any combination. We cannot study this structure in detail, but must take it into account in any fit.

We fit this distribution with a sum of two incoherent resonances and a non-resonant (NR) component. The $K^*(892)^0$ is described by a relativistic P-wave Breit-Wigner (BW) function with a threshold term, with mass and width fixed to the world-average values [21]. The NR function is the product of a fifth-order polynomial in the inverse of the mass and an exponential cutoff at threshold. The second peak is described by a relativistic D- or S-wave BW with parameters fixed to the nominal values [21] for $K_2^*(1430)$ or $K_0^*(1430)$. The narrower $K_2^*(1430)$ gives better fits here and in most cases below, so we use it everywhere. The result of the fit is shown as the line in Fig. 8(a), with the NR component indicated by the hatched area.

The fit yields 1671 ± 60 $K^*(892)^0 K^\pm\pi^\mp$ events and 85 ± 24 $K_2^*(1430)^\star K^\pm\pi^\mp$ events, where the uncertainties are statistical only. We do not claim observation of any particular state near 1.43 GeV/c^2, but we quote a generic number of events from this fit and those below for completeness. Some of the $K^{*0}(892)K^\pm\pi^\mp$ events are produced through the $K^{*0}(892)\overline{K}^{*0}$ channel, which we study below. In order to avoid double counting, we subtract the latter yield to obtain 1533 ± 60 quasi-three-body $K^*(892)^0 K^\pm\pi^\mp$ events.

The projection of Fig. 7(a) onto the horizontal axis is shown in Fig. 8(b), along with the results of a corresponding fit, which, after $K^{*0}(892)\overline{K}^{*0}(892)$ subtraction,

TABLE II: Measurements of the $e^+e^- \to K_S^0 K^\pm \pi^\mp \pi^0$ cross section versus $E_{c.m.} = m(K_S^0 K^\pm \pi^\mp \pi^0)$. The uncertainties are statistical only; systematic uncertainties are given in Table I.

$E_{c.m.}$ (GeV)	σ (nb)	$E_{c.m.}$ (GeV)	σ (nb)	$E_{c.m.}$ (GeV)	σ (nb)	$E_{c.m.}$ (GeV)	σ (nb)	$E_{c.m.}$ (GeV)	σ (nb)	$E_{c.m.}$ (GeV)	σ (nb)
1.51	0.05 ± 0.03	2.01	1.65 ± 0.16	2.51	0.65 ± 0.09	3.01	0.47 ± 0.07	3.61	0.14 ± 0.03
1.53	0.05 ± 0.03	2.03	1.67 ± 0.16	2.53	0.77 ± 0.10	3.03	0.26 ± 0.05	3.63	0.07 ± 0.02
1.55	0.02 ± 0.02	2.05	1.62 ± 0.16	2.55	0.83 ± 0.10	3.05	0.33 ± 0.06	3.65	0.15 ± 0.04
1.57	0.06 ± 0.04	2.07	1.91 ± 0.17	2.57	0.71 ± 0.09	3.07	0.39 ± 0.06	3.67	0.11 ± 0.03
1.59	0.19 ± 0.06	2.09	1.44 ± 0.15	2.59	0.85 ± 0.10	3.09	2.69 ± 0.16	3.69	0.17 ± 0.04
1.61	0.16 ± 0.06	2.11	1.90 ± 0.17	2.61	0.56 ± 0.08	3.11	1.61 ± 0.13	3.71	0.16 ± 0.04
1.63	0.36 ± 0.09	2.13	1.78 ± 0.16	2.63	0.43 ± 0.07	3.13	0.38 ± 0.06	3.73	0.07 ± 0.02
1.65	0.53 ± 0.10	2.15	1.73 ± 0.16	2.65	0.56 ± 0.08	3.15	0.30 ± 0.05	3.75	0.08 ± 0.02
1.67	0.52 ± 0.10	2.17	1.36 ± 0.14	2.67	0.64 ± 0.09	3.17	0.25 ± 0.05	3.77	0.08 ± 0.03
1.69	0.72 ± 0.12	2.19	1.49 ± 0.14	2.69	0.46 ± 0.07	3.19	0.16 ± 0.04	3.79	0.05 ± 0.02
1.71	0.70 ± 0.12	2.21	1.42 ± 0.14	2.71	0.63 ± 0.08	3.21	0.21 ± 0.04	3.81	0.09 ± 0.03
1.73	1.09 ± 0.14	2.23	1.36 ± 0.14	2.73	0.49 ± 0.07	3.23	0.18 ± 0.04	3.83	0.07 ± 0.02
1.75	0.91 ± 0.13	2.25	1.36 ± 0.14	2.75	0.59 ± 0.08	3.25	0.19 ± 0.04	3.85	0.04 ± 0.02
1.77	1.11 ± 0.14	2.27	1.15 ± 0.12	2.77	0.37 ± 0.06	3.27	0.23 ± 0.05	3.87	0.04 ± 0.02
1.79	1.48 ± 0.16	2.29	0.99 ± 0.12	2.79	0.51 ± 0.07	3.29	0.16 ± 0.04	3.89	0.11 ± 0.03
1.81	1.35 ± 0.15	2.31	0.95 ± 0.11	2.81	0.35 ± 0.06	3.31	0.19 ± 0.04	3.51	0.05 ± 0.02
1.83	1.67 ± 0.17	2.33	1.25 ± 0.13	2.83	0.30 ± 0.06	3.33	0.07 ± 0.03	3.53	0.17 ± 0.04
1.85	1.73 ± 0.17	2.35	0.98 ± 0.11	2.85	0.36 ± 0.06	3.35	0.15 ± 0.04	3.55	0.09 ± 0.03
1.87	1.98 ± 0.18	2.37	0.98 ± 0.11	2.87	0.42 ± 0.07	3.37	0.13 ± 0.03	3.57	0.08 ± 0.03
1.89	2.12 ± 0.19	2.39	0.61 ± 0.09	2.89	0.28 ± 0.05	3.39	0.12 ± 0.03	3.59	0.13 ± 0.03
1.91	1.99 ± 0.18	2.41	1.08 ± 0.12	2.91	0.44 ± 0.07	3.41	0.14 ± 0.03	3.91	0.08 ± 0.02
1.93	2.31 ± 0.19	2.43	0.84 ± 0.10	2.93	0.37 ± 0.06	3.43	0.15 ± 0.04	3.93	0.08 ± 0.03
1.95	2.05 ± 0.18	2.45	1.03 ± 0.11	2.95	0.23 ± 0.05	3.45	0.18 ± 0.04	3.95	0.05 ± 0.02
1.97	2.32 ± 0.19	2.47	0.93 ± 0.11	2.97	0.29 ± 0.06	3.47	0.09 ± 0.03	3.97	0.10 ± 0.03
1.99	2.00 ± 0.18	2.49	0.77 ± 0.10	2.99	0.42 ± 0.07	3.49	0.14 ± 0.04	3.99	0.08 ± 0.02

yields 454 ± 60 $K^*(892)^0 K_S^0 \pi^0$ and 20 ± 25 $K_2^*(1430) K_S^0 \pi^0$ events, respectively.

Corresponding fits to the projections of Fig. 7(b), shown in Figs. 8(c) and 8(d), followed by $K^*(892)^+ K^*(892)^-$ subtraction, yield 1173 ± 64 $K^*(892)^\pm K^\mp \pi^0$ events, 157 ± 50 $K^*(892)^\pm K_S^0 \pi^\mp$ events, 187 ± 25 $K_2^*(1430) K^\mp \pi^0$ events, and 141 ± 27 $K_2^*(1430) K_S^0 \pi^\mp$ events. The uncertainties are statistical only; systematic uncertainties are discussed below.

Repeating these fits in 0.2 GeV bins of $E_{c.m.}$, and using Eq. (3), we extract the cross sections for the processes $e^+e^- \to K^*(892)^0 K^\pm \pi^\mp$, $K^*(892)^0 \to K_S^0 \pi^0$, and $e^+e^- \to K^*(892)^0 K_S^0 \pi^0$, $K^*(892)^0 \to K^\pm \pi^\mp$ shown in Fig. 9(a), as well as for the processes $e^+e^- \to K^*(892)^\pm K_S^0 \pi^\mp$, $K^*(892)^\pm \to K^\pm \pi^0$ and $e^+e^- \to K^*(892)^\pm K^\mp \pi^0$, $K^*(892)^\pm \to K_S^0 \pi^\mp$ shown in Fig. 9(b). They are similar in size and shape, except that the $K^{*0} K_S^0 \pi^0$ cross section is a factor of 2 – 3 lower. Accounting for the $K^*(892)$ branching fractions, the $K^*(892)^0 K^\pm \pi^\mp$ and $K^*(892)^\pm K^\mp \pi^0$ cross sections are consistent with those we measured previously [8] in the $K^+K^-\pi^+\pi^-$ and $K^+K^-\pi^0\pi^0$ final states, respectively, and the $K^*(892)^\pm K_S^0 \pi^\mp$ cross section is consistent with our previous measurement [9] in the $K_S^0 K_S^0 \pi^+\pi^-$ final state.

We investigate the correlated production of K^{*0} and $\overline{K}^{*0}$ directly by repeating the fit of the $K^\pm \pi^\mp$ invariant mass distribution in 0.05 GeV/c^2 bins of the $K_S^0 \pi^0$ in-

variant mass. The resulting numbers of $K^*(892)^0$ decays in each bin are shown in Fig. 10(a), and there is a substantial peak near 892 MeV/c^2. Fitting these points with the same NR function plus a single BW function yields 138 ± 16 $e^+e^- \to K^{*0}\overline{K}^{*0}$ events. Similarly, fitting the $K_S^0 \pi^\pm$ invariant-mass distribution in bins of the $K^\pm \pi^0$ invariant mass yields the results for $K^*(892)^\pm$ decays shown in Fig. 10(b), and a single-resonance plus NR fit to those results yields 814 ± 36 $e^+e^- \to K^*(892)^+ K^*(892)^-$ events. Repeating this procedure in 0.2 GeV/c^2 bins of $E_{c.m.}$, and applying Eq. (3) provides the cross sections for $e^+e^- \to K^{*0}\overline{K}^{*0} \to K_S^0 K^\pm \pi^\mp \pi^0$ and $e^+e^- \to K^*(892)^\pm K^*(892)^\mp \to K_S^0 K^\pm \pi^\mp \pi^0$ shown in Figs. 9(a) and 9(b), respectively.

The $K^*(892)^+ K^*(892)^-$ intermediate state dominates both $K^*(892)^\pm K_S^0 \pi^\mp$ and $K^*(892)^\pm K^\mp \pi^0$ production, whereas the $K^{*0}\overline{K}^{*0}$ intermediate state (Fig. 9(a)) provides a significant fraction of $K^*(892)^0 K\pi$ production only near 2.1 GeV. Accounting for the $K^*(892)$ branching fractions, the $K^*(892)^+ K^*(892)^-$ cross section is consistent with our previous measurement [8] in the $K^+K^-\pi^0\pi^0$ final state, where it also dominated $K^*(892)^\pm K^\mp \pi^0$ production, and the $K^{*0}\overline{K}^{*0}$ cross section is consistent with our previous measurement [8] in the $K^+K^-\pi^+\pi^-$ final state, where it also represented only a small fraction of $K^*(892)^0 K^+\pi^-$ and $\overline{K}^{*0} K^-\pi^+$ production.

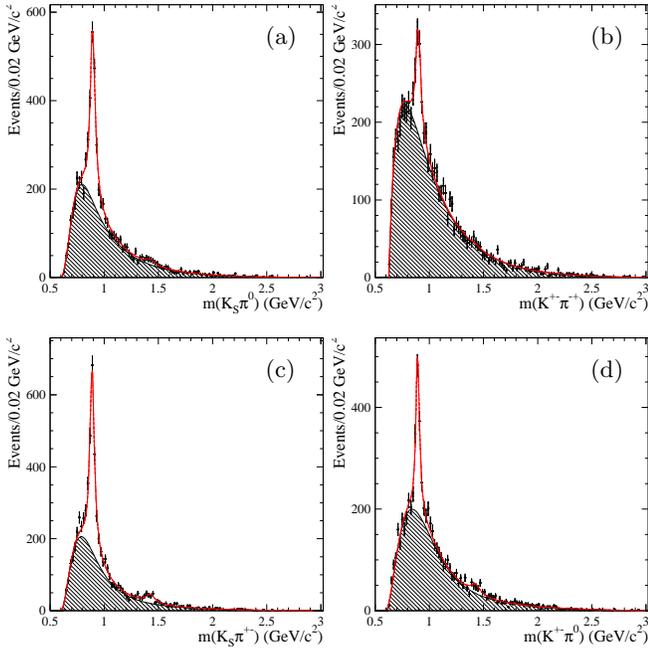Figure 11(a) shows the distribution of the $\pi^\pm \pi^0$

FIG. 8: The (a) $K_S^0\pi^0$ and (b) $K^\pm\pi^\mp$ invariant mass projections of Fig. 7(a), and the (c) $K_S^0\pi^\pm$ and (d) $K^\pm\pi^0$ invariant mass projections of Fig. 7(b). The lines represent the results of the fits described in the text, with the hatched areas denoting their non-resonant components.
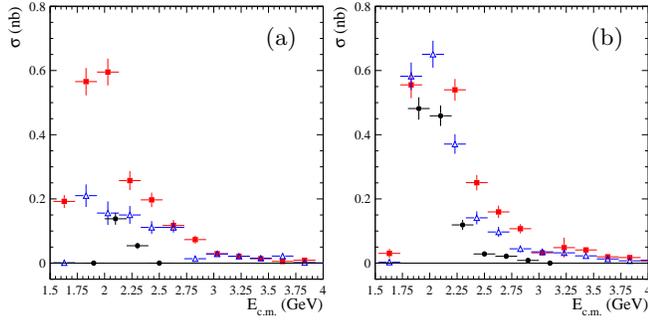

FIG. 9: Cross sections for (a) the processes $e^+e^- \to K^{*0}K^\pm\pi^\mp$(squares), $e^+e^- \to K^{*0}K_S^0\pi^0$(triangles), and $e^+e^- \to K^{*0}\overline{K}^{*0}$(circles), and (b) the processes $e^+e^- \to K^*(892)^\pm K_S^0\pi^\mp$(squares), $e^+e^- \to K^*(892)^\pm K^\mp\pi^0$ (triangles), and $e^+e^- \to K^*(892)^+K^*(892)^-$ (circles). The uncertainties are statistical only, and in each case the $K^*\overline{K}^*$ cross section is included in both of the others.

invariant mass in selected, background-subtracted, $K_S^0K^\pm\pi^\mp\pi^0$ events, which features a prominent $\rho(770)$ peak. The limited size of the data sample precludes a detailed study of the ρ region, and insteaad we perform a simple fit, using the the same NR function plus a relativistic P-wave BW with parameters fixed to those of the $\rho(770)^\pm$ [21]. The result is shown as the line and hatched area in Fig. 11(a). The fitted number of $K_S^0K^\pm\rho^\mp$ events, 2498 ± 100, is a large fraction of the $K_S^0K^\pm\pi^\mp\pi^0$ signal.
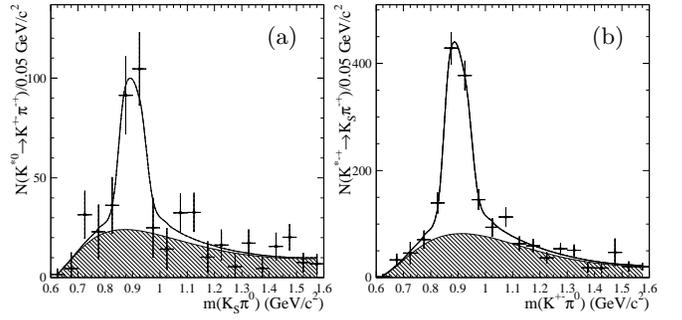
FIG. 10: The number of events in the $K_S^0K^\pm\pi^\mp\pi^0$ sample containing (a) a $K^{*0} \to K^\pm\pi^\mp$ decay as a function of the $K_S^0\pi^0$ invariant mass, and (b) a $K^*(892)^\pm \to K_S^0\pi^\pm$ decay as a function of the $K^\pm\pi^0$ invariant mass. The lines represent the result of the fits described in the text, with the hatched areas denoting their non-resonant components.
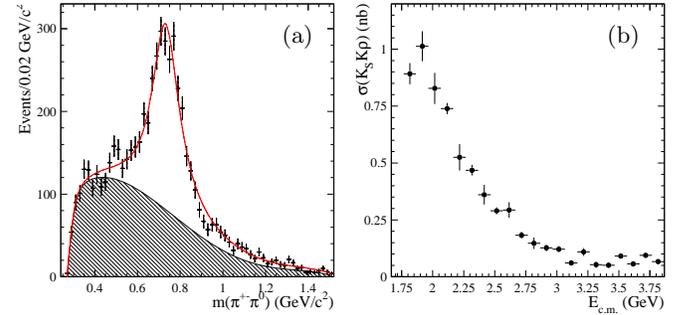

FIG. 11: (a) The $\pi^\pm\pi^0$ invariant-mass distribution in $e^+e^- \to K_S^0K^\pm\pi^\mp\pi^0$ events. The line represents the result of the fit described in the text, with the hatched area denoting its non-resonant component. (b) Cross section for the process $e^+e^- \to K_S^0K^\pm\rho^\mp$ as a function of $E_{\rm c.m.}$. The uncertainties are statistical only.

Again, the uncertainty is statistical only, and systematic uncertainties, discussed below, are large.

Repeating this fit in 0.1 GeV bins of $E_{\rm c.m.}$ and using Eq. (3), we extract the cross section for the process $e^+e^- \to K_S^0K^\pm\rho^\mp$, shown in Fig. 11(b). It peaks at lower $E_{\rm c.m.}$ and at approximately twice the value of a typical $K^*(892)K\pi$ cross section, and is consistent with our previous measurement of the $K^+K^-\rho^0$ cross section [8].

Some of these events may arise from $e^+e^- \to KK_1$ events, with $K_1 \to K\rho^\pm$, $\rho^\pm \to \pi^\pm\pi^0$. Figures 12(a) and (b) show the $K^\pm\pi^\mp\pi^0$ and $K_S^0\pi^\pm\pi^0$ invariant-mass distributions, respectively. There is some apparent structure in the peak regions of both distributions, and, as an exercise, we perform fits to each distribution with a sum of the same NR function and three incoherent P-wave BW functions with parameters fixed to world-average [21] values for the $K_1(1270)$, $K_1(1400)$, and $K_1(1650)$ resonances. We note that other nearby resonances, such as $K_2^*(1430)$ or $K^*(1680)$, could contribute in addition or instead. The results are shown as the lines
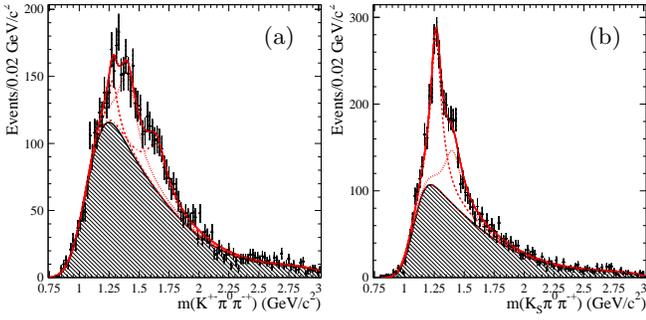
FIG. 12: The (a) $K^\pm\pi^\mp\pi^0$ and (b) $K_S^0\pi^\pm\pi^0$ invariant mass distributions in $e^+e^- \to K_S^0 K^\pm\pi^\mp\pi^0$ events. The solid lines represent the results of the fits described in the text; the hatched areas denote their non-resonant components, while the dashed, dotted, and dash-dotted lines indicate the contributions from $KK_1(1270)$, $KK_1(1400)$, and $KK_1(1650)$ events, respectively.

TABLE III: Summary of intermediate processes contributing to the $K_S^0 K^\pm\pi^\mp\pi^0$ final state. The results for the $K^*K\pi$ channels do not include contributions from the $K^*\overline{K}^*$ channels. The first uncertainty is statistical and the second systematic.

Intermediate state	Number of events				
$K^{*0}K_S^0\pi^0$	454	$\pm$	60	$\pm$	74
$K^{*0}K^\pm\pi^\mp$	1533	$\pm$	60	$\pm$	296
$K_2^*(1430)^0K_S^0\pi^0$	20	$\pm$	25	$\pm$	4
$K_2^*(1430)^0K^\pm\pi^\mp$	85	$\pm$	24	$\pm$	18
$K^*(892)^\pm K_S^0\pi^\mp$	157	$\pm$	50	$\pm$	117
$K^*(892)^\pm K^\mp\pi^0$	1173	$\pm$	64	$\pm$	170
$K_2^*(1430)^\pm K_S^0\pi^\mp$	141	$\pm$	27	$\pm$	28
$K_2^*(1430)^\pm K^\mp\pi^0$	187	$\pm$	25	$\pm$	35
$K^{*0}\overline{K}^{*0}$	138	$\pm$	16	$\pm$	55
$K^*(892)^+K^*(892)^-$	814	$\pm$	36	$\pm$	229
$K_S^0K^\pm\rho(770)^\mp$	2498	$\pm$	100	$\pm$	521
Total	7013	$\pm$	167	$\pm$	682

in Fig. 12, with the hatched areas denoting the NR components. The fit to the spectrum in Fig. 12(a) yields 230 ± 70 $K_S^0K_1(1270)^0$ events, 739 ± 101 $K_S^0K_1(1400)^0$ events, and 537 ± 126 $K_S^0K_1(1650)^0$ events, where all uncertainties are statistical only. The fit to Fig. 12(b) yields 1593 ± 76 $K^\pm K_1(1270)^\mp$ events, 547 ± 60 $K^\pm K_1(1400)^\mp$ events, and 0 ± 49 $K^\pm K_1(1650)^\mp$ events. Systematic uncertainties, discussed below, are large, but at least three (two) neutral (charged) K_1 states are required to describe the data. Far more charged than neutral $KK_1(1270)$, but far fewer charged than neutral $KK_1(1650)$, are produced.

Systematic uncertainties are substantial and difficult to evaluate. The NR function must describe a distribution complicated by resonances in, and kinematic constraints on, the other particles in the event, and the widths and positions of the $\rho(770)$ and $K^*(890)$ resonances do not allow strong constraints from the data. We adopt a simple, conservative procedure, based on the largest sources of variation. We repeat each fit with the NR function reduced to a fourth-order polynomial, and, separately, with the parameters of each resonance under study allowed to vary. The two resulting differences in yield are added in quadrature. To this we add, linearly, a 10% relative uncertainty to account for possible interference between resonances, the use of fixed vs. energy-dependent widths, and the choice of parametrization for the $\rho^\pm$ lineshape. This procedure is applied to the $E_{\text{c.m.}}$-integrated distributions in Figs. 8, 10, and 11(a), yielding systematic uncertainties in the respective total yields. In each case, the same relative uncertainty is applied as an overall normalization uncertainty in the cross sections (Figs. 9 and 11(b)).

The total yields of all measured $K^*K\pi$, $K^{*0}\overline{K}^{*0}$, and $KK\rho$ intermediate states and their uncertainties are listed in Table III. We do not quote yields for any of the KK_1 modes, as the uncertainties are very large. Here, we have subtracted each $K^*\overline{K}^*$ yield from both of the relevant $K^*K\pi$ yields, so that the sum of all yields,

7013 ± 683 events, can be compared with the total number of $K_S^0K^\pm\pi^\mp\pi^0$ events, which is 6430 ± 90. The two numbers are consistent, leaving little room for additional resonant contributions.

From Table III we see that $K^*(892)^+K^*(892)^-$ events account for most of the $K^*(892)^\pm K_S^0\pi^\mp$ production, but only half the $K^*(892)^\pm K^\mp\pi^0$ production. Neutral $K^*(892)$ pair production is much lower than charged, whereas $K^{*0}K\pi$ and $K^*(892)^\pm K\pi$ are similar. The rate of charged $K^*(892)^+K^*(892)^-$ production is about three times that of neutral $K^{*0}\overline{K}^{*0}$, and these are about four and fifteen times lower than those of the respective $K^*(892)$ states. This pattern in the data after $q\overline{q}$ background subtraction is consistent with that seen in our previous study of $e^+e^- \to K^+K^-\pi^+\pi^-$ and $K^+K^-\pi^0\pi^0$ [8].

V. THE $K_S^0K^\pm\pi^\mp\eta$ FINAL STATE

A. Event selection

The $\chi^2_{K_S^0K^\pm\pi^\mp\eta}$ distribution for the selected $e^+e^- \to K_S^0K^\pm\pi^\mp\eta$ events in the data is shown in Fig. 13, together with the corresponding distributions of simulated signal and $q\overline{q}$ background events. Again, the $q\overline{q}$ background is normalized using the π^0 peaks in the data and simulated invariant-mass distributions of the ISR photon candidate combined with all other photon candidates in the event. The signal simulation is normalized to have the same integral in the first five bins as the data minus the $q\overline{q}$ background. We define signal and control regions by $\chi^2_{K_S^0K^\pm\pi^\mp\eta} < 20$ and $20 < \chi^2_{K_S^0K^\pm\pi^\mp\eta} < 40$, respectively, containing 459 (1418) and 128 (147) data (simulated) events.

Figure 14(a) compares the $\gamma\gamma$ invariant-mass distribution of the η candidate for data events in the signal
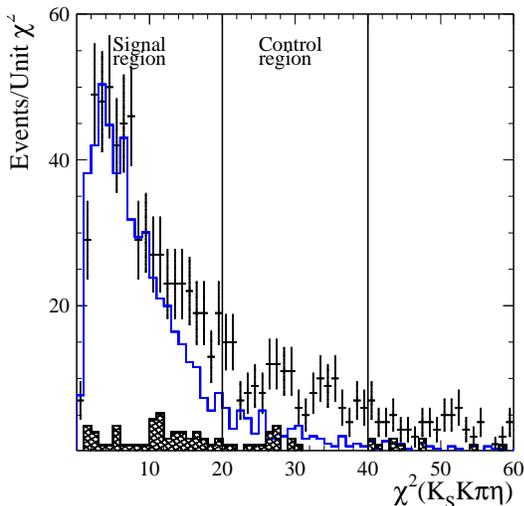
FIG. 13: Distribution of χ^2 from the 5-constraint fit of the $K_S^0 K^{\pm}\pi^{\mp}\eta\gamma$ candidates in the data (points). The open and cross-hatched histograms are the distributions for simulated signal and $q\bar{q}$ background events, respectively, normalized as described in the text. The signal and control regions are indicated.
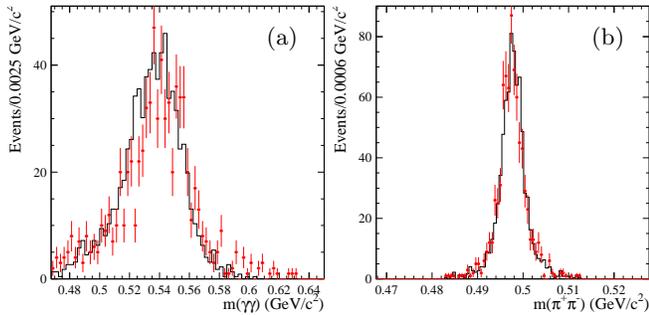

FIG. 14: The (a) $\gamma\gamma$ and (b) $\pi^+\pi^-$ invariant-mass distributions of the η and K_S^0 candidates, respectively, in $K_S^0 K^{\pm}\pi^{\mp}\eta$ events in the $\chi^2_{K_S^0 K^{\pm}\pi^{\mp}\eta}$ signal region, for the selected data (points) and the signal simulation (histograms).

region with the prediction of the signal-event simulation, and Fig. 14(b) shows the corresponding $\pi^+\pi^-$ invariant-mass distributions of the K_S^0 candidate. The η peak is wider and more skewed than the π^0 peak in Fig. 2(a), but the selection criteria are sufficiently loose that there is no effect on the results.

The distribution of the invariant mass of the final-state hadronic system for data events in the signal region is shown in Fig. 15. A narrow peak due to $J/\psi \rightarrow K_S^0 K^{\pm}\pi^{\mp}\eta$ decays is visible. The $q\bar{q}$ background is shown as the cross-hatched histrogram. We subtract it and then estimate the remaining background, assumed to arise from ISR events, as described above. We take the shape of the ISR background χ^2 distribution directly from the data, as the difference between experimental $\chi^2_{K_S^0 K^{\pm}\pi^{\mp}\eta}$

distribution with $q\bar{q}$ background subtracted and that of the normalized signal simulation (points and open histogram in Fig. 13).

The total number of signal events obtained in this way is 358 ± 24 (stat.) We define the systematic uncertainty in two $E_{\text{c.m.}}$ regions to be half the number of background events, resulting in a relative uncertainty in the signal event yields of 11% for $E_{\text{c.m.}} < 3$ GeV and 18% for $E_{\text{c.m.}} > 3$ GeV.

B. Detection efficiency

The total reconstruction and selection efficiency from the signal simulation is shown as a function of $E_{\text{c.m.}}$ in Fig. 16, and is parametrized by a smooth function, shown as the solid line. We apply the same corrections for charged-track finding, K_S^0 reconstruction, and $K^{\pm}$ and $\pi^{\pm}$ identification efficiencies as in Sec. IV B, and evaluate a correction for the shape of the χ^2 distribution in the same way. We do not have a dedicated study of η reconstruction efficiency, so we assume a correction equal to that on the π^0 efficiency, but with the uncertainty doubled.

The momentum and polar angle distributions of the K_S^0, $K^{\pm}$, $\pi^{\pm}$, and η candidates in the data are well described by the signal simulation. To study the effects of resonant substructure, we use fast simulations of signal and the ISR $K^*(892)^{\pm}K^{\mp}\eta$ and $K^*(892)^0 K_S^0\eta$ processes. Their efficiencies are consistent and we take the largest difference, which is 2.5%, as the systematic uncertainty at all $E_{\text{c.m.}}$, to account for potential differences between data and simulation for the $E_{\text{c.m.}}$ dependence of the effi-
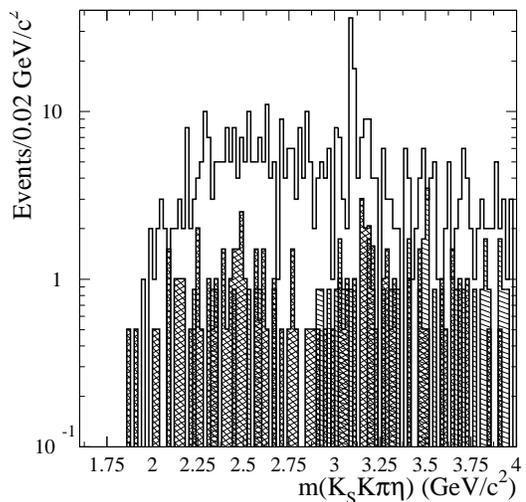

FIG. 15: Distribution of the fitted $K_S^0 K^{\pm}\pi^{\mp}\eta$ invariant mass for data events in the signal region (open histogram). The hatched and cross-hatched distributions show the estimated backgrounds evaluated from the control region and from $q\bar{q}$ events, respectively.
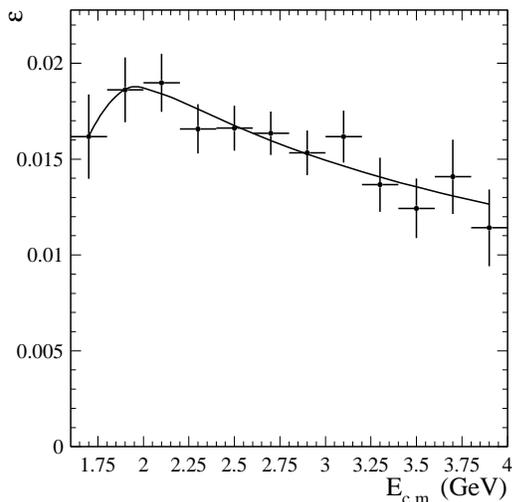
FIG. 16: Detection efficiency for $e^+e^- \rightarrow K_S^0 K^\pm \pi^\mp \eta$ events as a function of the hadronic invariant mass $E_{c.m.} = m(K_S^0 K^\pm \pi^\mp \eta)$. The solid curve shows the fitted parametrization.
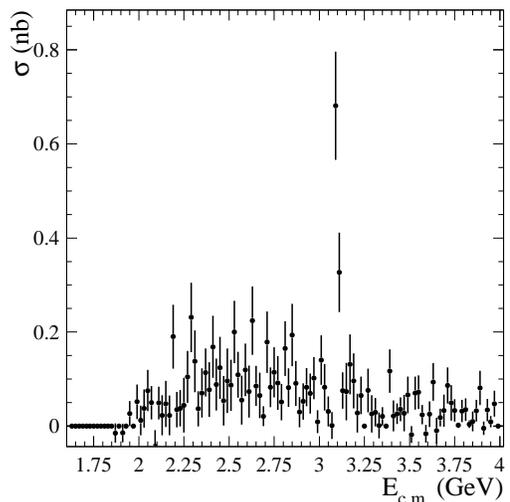

FIG. 17: Cross section for the process $e^+e^- \rightarrow K_S^0 K^\pm \pi^\mp \eta$. Uncertainties are statistical.

ciency and for the resonant structure. These corrections and their uncertainties are listed in Table IV. The total correction is $+0.6 \pm 5.5\%$.

C. Cross section for $e^+e^- \rightarrow K_S^0 K^\pm \pi^\mp \eta$

The $e^+e^- \rightarrow K_S^0 K^\pm \pi^\mp \eta$ cross section is obtained from the analog of Eq. (3), with the π^0 replaced by an η. The differential luminosity is the same as for the $K_S^0 K^\pm \pi^\mp \pi^0$ cross section, and the radiative correction is evaluated in the analagous way to be R=1.0022±0.0016, independent of $E_{c.m.}$.

The fully corrected cross section is shown in Fig. 17 and listed in Table V, with statistical uncertainties only. The relative systematic uncertainties are summarized in Table IV, yielding a total systematic uncertainty of 12.0% for $E_{c.m.} < 3$ GeV and 19% for $E_{c.m.} > 3$ GeV.

TABLE IV: Summary of the corrections to, and systematic uncertainties in, the $e^+e^- \rightarrow K_S^0 K^\pm \pi^\mp \eta$ cross section.

Source	Correction (%)	Systematic uncertainty (%)
η efficiency	+2.0	2.0
$K^\pm$, $\pi^\pm$ reconstruction	+1.6	2.0
K_S^0 reconstruction	+1.1	1.0
PID efficiency	0.0	2.0
χ^2 selection	-4.0	4.6
Background subtraction	—	11.0, <3.0 GeV
		18.0, >3.0 GeV
Model acceptance	—	2.5
Luminosity and Rad.Corr.	—	1.4
Total	+0.6	12.8, <3.0 GeV
		19.1, >3.0 GeV

D. Substructure in $K_S^0 K^\pm \pi^\mp \eta$

We study substructure in the $K_S^0 K^\pm \pi^\mp \eta$ mode in the same way as for the $K_S^0 K^\pm \pi^\mp \pi^0$ mode, using background-subtracted data and excluding the J/ψ region $3.0 < E_{c.m.} < 3.2$ GeV. Here, we expect far less structure, and indeed we see no significant structure in the $K^\pm K_S^0$, $K^\pm \eta$, or $K_S^0 \eta$ invariant-mass distributions. Figure 18 shows the $K_S^0 \pi^\pm$ and $K^\pm \pi^\mp$ invariant-mass distributions. The former shows a dominant $K^*(892)^\pm$ peak, as well as structure near 1.43 GeV/c^2, whereas the latter shows only a modest $K^*(892)^0$ peak over a large, broad distribution.

We fit the $m(K_S^0 \pi^\pm)$ distribution with a sum of incoherent $K^*(892)$ and $K_2^*(1430)$ resonances and a NR component of the same form as in Sec. IV D. The result of the fit is shown in Fig. 18(a) as the solid line, yielding 242±21 $e^+e^- \rightarrow K^*(892)^\pm K^\mp \eta$ events and 10±5 $e^+e^- \rightarrow K_2^*(1430)^\pm K^\mp \eta$ events, where the uncertainties are statistical only. There is no hint of a $K_2^*(1430)^0$ signal in the $m(K^\pm \pi^\mp)$ distribution, and we show the result of a single-resonance+NR fit in Fig. 18(b), which yields 123±36(stat.) $e^+e^- \rightarrow K^*(892)^0 K_S^0 \eta$ events.

We estimate systematic uncertainties due to the fitting procedure as above, and summarize these results in Table VI. The sum of these three resonant yields is consistent with the total number of $K_S^0 K^\pm \pi^\mp \eta$ events, and the suppression of neutral with respect to charged $K^*(892)$ production is similar to that seen above in the $K_S^0 K^\pm \pi^\mp \pi^0$ final state, and in our previous study of the $K^+ K^- \pi^+ \pi^-$ final state [8].

Repeating these fits in 0.2 GeV bins of $E_{c.m.}$, and using Eq. (3), we extract cross sections for the processes $e^+e^- \rightarrow K^*(892)^\pm K^\mp \eta$ with $K^*(892)^\pm \rightarrow K_S^0 \pi^\pm$, and $e^+e^- \rightarrow K^*(892)^0 K_S^0 \eta$ with $K^*(892)^0 \rightarrow K^\pm \pi^\mp$. These

TABLE V: Measurement of $e^+e^- \to K_S^0 K^\pm \pi^\mp \eta$ cross section. The uncertainties are statistical only; systematic uncertainties are given in Table IV.

| $E_{c.m.}$ (GeV)	σ (nb)	$E_{c.m.}$ (GeV)	σ (nb)	$E_{c.m.}$ (GeV)	σ (nb)	$E_{c.m.}$ (GeV)	σ (nb)
2.01	0.01 ± 0.03	2.51	0.09 ± 0.05	3.01	0.14 ± 0.05	3.51	-0.02 ± 0.02
2.03	0.04 ± 0.04	2.53	0.20 ± 0.07	3.03	0.08 ± 0.05	3.53	0.07 ± 0.04
2.05	0.08 ± 0.04	2.55	0.11 ± 0.05	3.05	0.03 ± 0.03	3.55	0.07 ± 0.04
2.07	0.05 ± 0.04	2.57	0.06 ± 0.05	3.07	0.00 ± 0.03	3.57	0.02 ± 0.02
2.09	-0.04 ± 0.03	2.59	0.12 ± 0.06	3.09	0.68 ± 0.11	3.59	-0.02 ± 0.02
2.11	0.05 ± 0.03	2.61	0.07 ± 0.06	3.11	0.33 ± 0.08	3.61	0.03 ± 0.03
2.13	0.02 ± 0.04	2.63	0.22 ± 0.07	3.13	0.08 ± 0.04	3.63	0.09 ± 0.04
2.15	0.05 ± 0.05	2.65	0.09 ± 0.04	3.15	0.07 ± 0.06	3.65	-0.01 ± 0.03
2.17	0.02 ± 0.04	2.67	0.07 ± 0.05	3.17	0.13 ± 0.06	3.67	0.02 ± 0.02
2.19	0.19 ± 0.07	2.69	0.02 ± 0.02	3.19	0.10 ± 0.06	3.69	0.03 ± 0.03
2.21	0.04 ± 0.04	2.71	0.18 ± 0.07	3.21	0.03 ± 0.04	3.71	0.09 ± 0.04
2.23	0.04 ± 0.04	2.73	0.08 ± 0.04	3.23	0.07 ± 0.04	3.73	0.05 ± 0.04
2.25	0.04 ± 0.06	2.75	0.11 ± 0.05	3.25	0.00 ± 0.00	3.75	0.03 ± 0.02
2.27	0.10 ± 0.06	2.77	0.09 ± 0.06	3.27	0.08 ± 0.05	3.77	0.00 ± 0.01
2.29	0.23 ± 0.07	2.79	0.05 ± 0.04	3.29	0.03 ± 0.04	3.79	0.03 ± 0.02
2.31	0.14 ± 0.07	2.81	0.16 ± 0.06	3.31	0.03 ± 0.03	3.81	0.04 ± 0.02
2.33	0.04 ± 0.04	2.83	0.08 ± 0.04	3.33	0.00 ± 0.03	3.83	0.00 ± 0.01
2.35	0.07 ± 0.05	2.85	0.19 ± 0.07	3.35	0.02 ± 0.02	3.85	0.01 ± 0.02
2.37	0.11 ± 0.05	2.87	0.09 ± 0.05	3.37	0.00 ± 0.00	3.87	0.03 ± 0.02
2.39	0.08 ± 0.06	2.89	0.03 ± 0.03	3.39	0.12 ± 0.05	3.89	0.08 ± 0.04
2.41	0.17 ± 0.07	2.91	0.05 ± 0.04	3.41	0.02 ± 0.03	3.91	0.00 ± 0.01
2.43	0.09 ± 0.06	2.93	0.08 ± 0.04	3.43	0.03 ± 0.02	3.93	0.03 ± 0.02
2.45	0.12 ± 0.07	2.95	0.07 ± 0.04	3.45	0.04 ± 0.03	3.95	0.01 ± 0.01
2.47	0.05 ± 0.05	2.97	0.10 ± 0.05	3.47	0.03 ± 0.04	3.97	0.05 ± 0.03
2.49	0.10 ± 0.07	2.99	0.01 ± 0.02	3.49	0.07 ± 0.04	3.99	0.00 ± 0.00
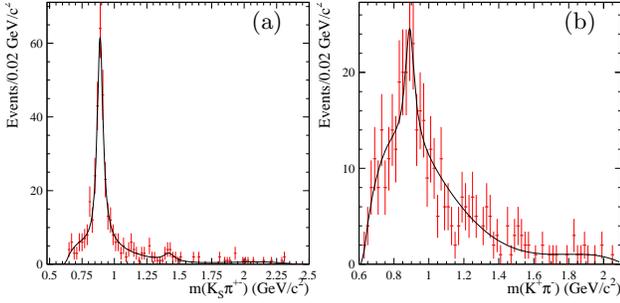
FIG. 18: The (a) $K_S^0 \pi^\pm$ and (b) $K^\pm \pi^\mp$ invariant-mass distributions in $e^+e^- \to K_S^0 K^\pm \pi^\mp \eta$ events. The lines represent the results of the fits described in the text.
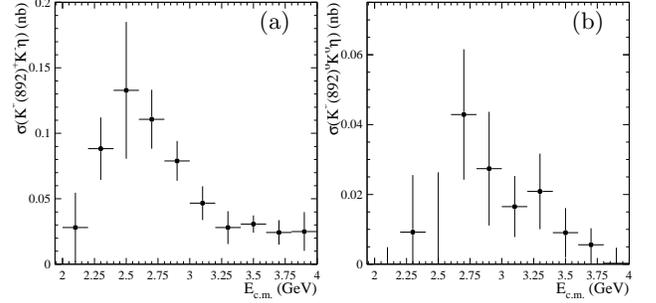

FIG. 19: Cross sections for the processes (a) $e^+e^- \to K^*(892)^\pm K^\mp \eta$ and (b) $e^+e^- \to K^*(892)^0 K_S^0 \eta$. The uncertainties are statistical only.

are shown in Fig. 19 with statistical uncertainties. A systematic uncertainty of 16% (21%) is applicable for $E_{\text{c.m.}}$ below (above) 3 GeV. These are the first measurements of these cross sections. Well above threshold, they become consistent with the corresponding $K^*(892)\overline{K}\pi^0$ cross sections.

VI. THE J/ψ REGION

Figures 20 and 21 show expanded views of the mass distributions in Figs. 3 and 15, respectively, in the 2.8–

TABLE VI: Summary of intermediate processes contributing to the $K_S^0 K^\pm \pi^\mp \eta$ final state.

Intermediate state	Number of events				
$K^{*0} K_S^0 \eta$	123	±	36	±	13
$K^*(892)^\pm K^\mp \eta$	242	±	21	±	24
$K_2^*(1430)^\pm K^\mp \eta$	10	±	5	±	2
Total	375	±	42	±	27

3.8 GeV/c^2 mass region. They show clear J/ψ signals, and no other significant structure. Fitting each of these
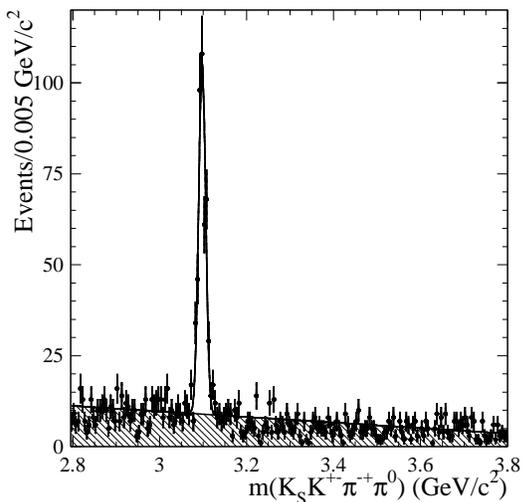
FIG. 20: The $K_S^0 K^\pm \pi^\mp \pi^0$ invariant-mass distribution in the J/ψ mass region. The line represents the result of the fit described in the text, with the open (hatched) area indicating the (non)resonant component.
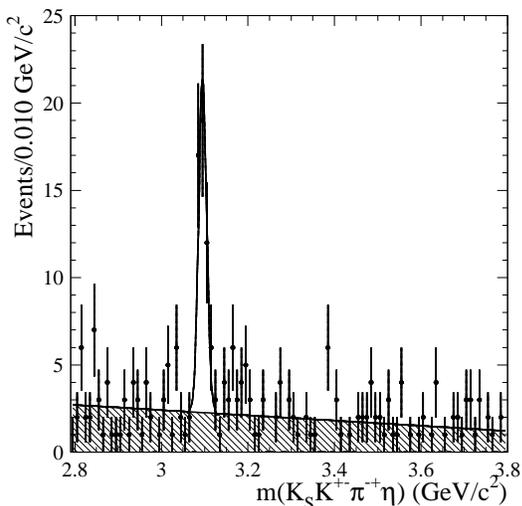

FIG. 21: The $K_S^0 K^\pm \pi^\mp \eta$ invariant-mass distribution in the J/ψ mass region. The line represents the result of the fit described in the text, with the open (hatched) area indicating the (non)resonant component.

distributions with the sum of a Gaussian describing the J/ψ signal shape and a first-order polynomial function yields 393 ± 23 $J/\psi \to K_S^0 K^\pm \pi^\mp \pi^0$ decays and 44 ± 7 $J/\psi \to K_S^0 K^\pm \pi^\mp \eta$ decays. In these fits, the Gaussian center is fixed to the nominal J/ψ mass [21], and the fitted widths of 8–9 MeV/c^2 are consistent with the simulated resolution. The results of the fits are shown as solid lines on Figs. 20 and 21, with the hatched areas representing the non-J/ψ components.

Using the simulated selection efficiencies with all the corrections described above and the differential luminos-

ity, and dividing by the $K_S^0 \to \pi^+ \pi^-$ and $\pi^0/\eta \to \gamma\gamma$ branching fractions [21], we calculate the products of the J/ψ electronic width and branching fractions to these modes, and list them in Table VII. The first uncertainties are statistical, and the second include all the systematic uncertainties applied to the cross sections, described above.

Using the world-average value of $\Gamma_{ee}^{J/\psi} = 5.55$ keV [21], we obtain the corresponding J/ψ branching fractions, also listed in Table VII. The results for $\mathcal{B}_{K_S^0 K^\pm \pi^\mp \pi^0}^{J/\psi}$ and $\mathcal{B}_{K_S^0 K^\pm \pi^\mp \eta}^{J/\psi}$ include the contributions of both nonresonant and intermediate resonant states. The systematic uncertainties now include the uncertainty in $\Gamma_{ee}^{J/\psi}$. Our result for $\mathcal{B}_{K_S^0 K^\pm \pi^\mp \eta}^{J/\psi}$ is consistent with, and more precise than, the world average value [21]. Our result for $\mathcal{B}_{K_S^0 K^\pm \pi^\mp \pi^0}^{J/\psi}$ is the first measurement of this branching fraction. Our result, $\mathcal{B}_{K_S^0 K^\pm \pi^\mp \pi^0}^{J/\psi} = (5.7 \pm 0.3 \pm 0.4) x 10^{-3}$, is consistent with our previous measurement of $\mathcal{B}_{K^+ K^- \pi^+ \pi^-}^{J/\psi} = (6.84 \pm 0.28) x 10^{-3}$ [8] within around two standard deviations, and larger than our $\mathcal{B}_{K^+ K^- \pi^0 \pi^0}^{J/\psi} = (2.12 \pm 0.21) \times 10^{-3}$ [8], $\mathcal{B}_{K_S^0 K_L^0 \pi^+ \pi^-}^{J/\psi} = (3.7 \pm 0.7) \times 10^{-3}$ [9], and $\mathcal{B}_{K_S^0 K_S^0 \pi^+ \pi^-}^{J/\psi} = (1.68 \pm 0.17) \times 10^{-3}$ [9].

A. Substructure in $J/\psi \to K_S^0 K^\pm \pi^\mp \pi^0$ decays

We study the $K_S^0 K^\pm \rho^\mp$ and $K^* K \pi$ contributions to the $J/\psi \to K_S^0 K^\pm \pi^\mp \pi^0$ decay in a manner similar to that described in Sec. IV D. Fitting the $\pi^\pm \pi^0$ invariant mass distribution (see Fig. 11(a)) in 10 MeV/c^2 bins of the $K_S^0 K^\pm \pi^\mp \pi^0$ invariant mass yields the numbers of $K_S^0 K^\pm \rho^\mp$ events per bin shown in Fig. 22. A fit to a Gaussian plus first-order polynomial (line and hatched area, respectively, in Fig. 22) yields $130 \pm 12 \pm 19$ $J/\psi \to K_S^0 K^\pm \rho^\mp$ decays, where the first uncertainty is statistical and the second is the systematic uncertainty associated with the fit to the $\pi^\mp \pi^0$ invariant-mass distribution, described above. We correct for efficiency, and calculate the product $\Gamma_{ee}^{J/\psi} \mathcal{B}_{K_S^0 K^\pm \rho^\mp}^{J/\psi}$ from which we determine the branching fraction. The results, listed in Table VII, represent the first measurement of this J/ψ decay mode.

We perform fits in bins of $E_{c.m.}$ between 3.0 and 3.2 GeV, analogous to those shown in Figs. 8 and 10, of the $K_S^0 \pi^0$, $K^\pm \pi^\mp$, $K_S^0 \pi^\pm$ and $K^\pm \pi^0$ invariant-mass distributions, to determine the number of respective $J/\psi \to K\pi$ decays. Systematic uncertainties for these results are determined as described in Sec. IV D. We fit each of the four distributions in Fig. 23 with a Gaussian plus first-order polynomial function to obtain $34 \pm 6 \pm 22$ $J/\psi \to K^{*0} K_S^0 \pi^0$ decays, $99 \pm 10 \pm 17$ $J/\psi \to K^{*0} K^\pm \pi^\mp$ decays, $80 \pm 10 \pm 24$ $J/\psi \to K^*(892)^\pm K^\mp \pi^0$ decays, and $64 \pm 9 \pm 22$ $J/\psi \to K^*(892)^\pm K_S^0 \pi^\mp$ decays. Here, the first uncertainties are statistical and the second system-

atic, where these latter terms result from the fit procedure. We correct for efficiency and calculate the products $\Gamma_{ee}^{J/\psi} \mathcal{B}_{K^*(892)\overline{K}\pi}^{J/\psi} \mathcal{B}_{K\pi}^{K^*(892)}$, and then the products of the J/ψ and $K^*(892)$ branching fractions, and list them in Table VII. With the current data samples, we are not able to study $J/\psi \to K^*\overline{K}^*$ decays.

There are no previous measurements of these decay chains. The measurement $\mathcal{B}_{K^*(892)^\pm K_S^0 \pi^\mp}^{J/\psi} \mathcal{B}_{K_S^0 \pi^\pm}^{K^*(892)^\pm} = (2.6 \pm 0.9) \times 10^{-3}$ [9] is about half as large as our result for $\mathcal{B}_{K_S^0 K^\pm \pi^\mp \pi^0}^{J/\psi}$; this difference is consistent with expectations for isospin conservation. In Ref. [8] it was found that the $K^+K^-\pi^+\pi^-$ mode is dominated by the $K^*(892)^0 K^\pm \pi^\mp$ channel, which originates predominantly from the decay of $K^{*0}(892)\overline{K}_{(0,2)}^*(1430)$ apart from a small contribution from $K^{*0}(892)\overline{K}^{*0}(892)$. Our results are consistent with this pattern, and the world-average $\mathcal{B}_{K^{*0}\overline{K}^{*0}}^{J/\psi} = (0.23 \pm 0.07) \times 10^{-3}$ [21] is well below our values for $\mathcal{B}_{K^{*0}(892)K\pi}^{J/\psi}$. On the other hand, the sum of our $\mathcal{B}_{K^*(892)^\pm K\pi}^{J/\psi}$ modes is only about twice the world-average $\mathcal{B}_{K^*(892)^\pm K^*(892)^\mp}^{J/\psi} = 1.00_{-0.40}^{+0.22} \times 10^{-3}$ [21].
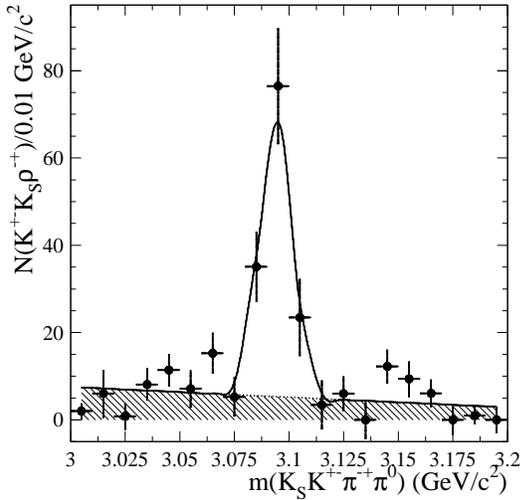

FIG. 22: The number of $K_S^0 K^\pm \rho^\mp$ events as a function of the $K_S^0 K^\pm \pi^\mp \pi^0$ invariant mass in the J/ψ region. The line represents the result of the fit described in the text, with the open (hatched) area indicating the resonant (nonresonant) component."

VII. SUMMARY

We have presented the first measurements of the $e^+e^- \to K_S^0 K^\pm \pi^\mp \pi^0$ and $e^+e^- \to K_S^0 K^\pm \pi^\mp \eta$ cross sections. The measurements are performed over the c.m. energy ranges from their respective threshold to 4 GeV. The total uncertainty in the $K_S^0 K^\pm \pi^\mp \pi^0$ cross section ranges from 6.3% at low masses, to 11.5% at 3 GeV, in-
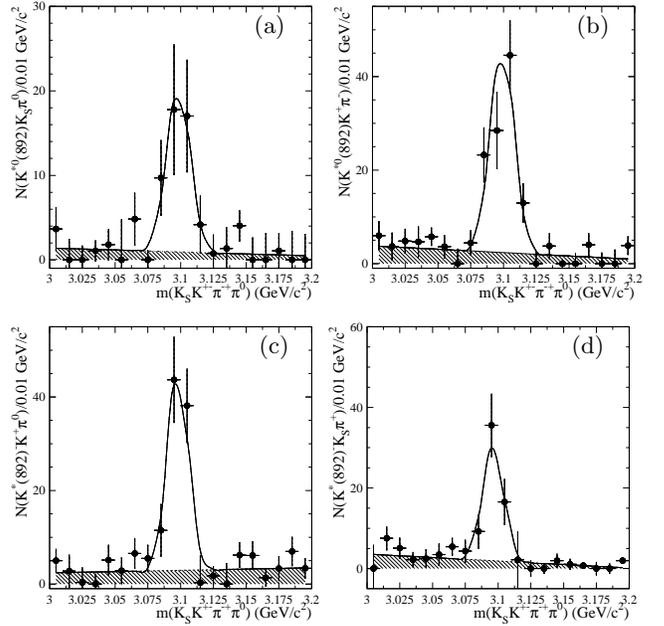

FIG. 23: Event yields of (a) $K^{*0}K_S^0\pi^0$, (b) $K^{*0}K^\pm\pi^\mp$, (c) $K^{*\pm}K^\mp\pi^0$, and (d) $K^{*\pm}K_S^0\pi^\mp$ final states as functions of the $K_S^0 K^\pm \pi^\mp \pi^0$ invariant mass in the J/ψ region. The lines represent the results of the fits described in the text, with the open (hatched) areas indicating the resonant (nonresonant) components.

creasing with higher masses. That on the $K_S^0 K^\pm \pi^\mp \eta$ cross section is 12.8% (19.1%) below (above) 3 GeV. These results are useful inputs into the total hadronic cross section, and the theoretical calculation of $(g-2)_\mu$.

The $K_S^0 K^\pm \pi^\mp \pi^0$ cross section exhibits a slow rise from threshold, then a steep rise from 1.6 GeV to a peak value of about 2 nb near 1.9 GeV, followed by a slow decrease with increasing mass. There is a clear J/ψ signal, but no other significant structure. The cross section is about half that of $e^+e^- \to K^+K^-\pi^+\pi^-$ [8], and about twice that of $e^+e^- \to K_S^0 K_L^0 \pi^+\pi^-$ [9] or $K^+K^-\pi^0\pi^0$ [8].

The $K_S^0 K^\pm \pi^\mp \eta$ cross section is much smaller, and consistent with zero between threshold and 2 GeV. It then demonstrates a slow rise to a value of about 0.1 nb over a wide range around 2.5 GeV, followed by a slow decrease with increasing mass. There is a clear J/ψ signal and no other significant structure.

Several intermediate resonant states are evident in the $K_S^0 K^\pm \pi^\mp \pi^0$ data, and we have measured cross sections into this final state via $e^+e^- \to K^{*0}\overline{K}^{*0}$, $K^{*0}K_S^0\pi^0$ + c.c., $K^{*0}K^-\pi^+$ + c.c., $K^*(892)^\pm K^*(892)^\mp$, $K^*(892)^\pm K_S^0\pi^\mp$, $K^*(892)^\pm K^\mp \pi^0$, and $K_S^0 K^\pm \rho^\mp$. There are also signals for the production of at least one $K^*(1430)$ state, and at least three K_1 states. Together, these channels dominate $K_S^0 K^\pm \pi^\mp \pi^0$ production, and the $K^*(892)^+K^*(892)^-$ channel dominates both $K^*(892)^\pm K_S^0 \pi^\mp$ and $K^*(892)^\pm K^\mp \pi^0$ production. The cross sections are consistent with previous results in other final states.

TABLE VII: Summary of J/ψ decay measurements from this analysis. Here, $\mathcal{B}_f$ represents the J/ψ branching fraction to the indicated final state and $\Gamma_{ee}^{J/\psi}$ the partial width for J/ψ decay to ee.

	This work		PDG(2014)
final state	$\mathcal{B}_f \cdot \Gamma_{ee}^{J/\psi}$ (eV)	$\mathcal{B}_f$ (10^{-3})	$\mathcal{B}_f$ (10^{-3})
$K_S^0\, K^\pm\, \pi^\mp\, \pi^0$	$31.7\pm1.9\pm1.8$	$5.7\pm0.3\pm0.4$	—
$K_S^0 K^\pm \pi^\mp \eta$	$7.3\pm1.4\pm0.4$	$1.30\pm0.25\pm0.07$	2.2 ± 0.4
$K_S^0 K^\pm \rho(770)^\mp$	$10.4\pm1.0\pm1.9$	$1.87\pm0.18\pm0.34$	—
$K^*(892)^0\ K^-\ \pi^+$ + c.c.	$7.1\pm0.8\pm1.2$	$1.3\pm0.1\pm0.2$	—
$K^*(892)^0\ K_S^0\ \pi^0$ + c.c.	$2.4\pm0.5\pm1.5$	$0.43\pm0.01\pm0.27$	—
$K^*(892)^\pm K^\mp \pi^0$	$5.7\pm0.7\pm1.7$	$1.0\pm0.1\pm0.3$	—
$K^*(892)^\pm K_S^0 \pi^\mp$	$4.6\pm0.6\pm1.6$	$0.8\pm0.1\pm0.3$	—

The $K_S^0 K^\pm \pi^\mp \eta$ final state includes contributions from $K^{*0} K_S^0 \eta + c.c.$, $K^*(892)^\pm K^\mp \eta$, and $K_2^*(1430)^\pm K^\mp \eta$, and no other significant substructure. We have obtained the first measurements of the $e^+e^- \to K^{*0} K_S^0 \eta + c.c.$ and $K^*(892)^\pm K^\mp \eta$ cross sections, and these channels dominate the overall $K_S^0 K^\pm \pi^\mp \eta$ production.

With the results of this analysis, BABAR has now provided the cross section measurements for the complete set of allowed $e^+e^- \to K\overline{K}\pi$ and $K\overline{K}\pi\pi$ processes except for those containing a $K_L^0 K_L^0$ pair. Since the latter modes are expected to be the same as the corresponding modes with a $K_S^0 K_S^0$ pair, the $K\overline{K}\pi$ and $K\overline{K}\pi\pi$ contributions to $g_\mu - 2$ can be calculated using this set of exclusive cross section measurements, with no assumptions or isospin relations. We expect a reduction in the total uncertainties of these contributions by a factor of five to eight compared with current estimates [1].

We have measured the J/ψ branching fraction to $K_S^0 K^\pm \pi^\mp \eta$, and presented the first J/ψ branching fraction measurement to $K_S^0 K^\pm \pi^\mp \pi^0$ as well as the branching fractions to the $K_S^0 K^\pm \pi^\mp \pi^0$ final state via $K^{*0} K^\pm \pi^\mp + c.c.$, $K^{*0} K_S^0 \pi^0 + c.c.$, $K^*(892)^+ K^- \pi^0 + c.c.$, $K^*(892)^\pm K_S^0 \pi^\mp$, and $K_S^0 K^\pm \rho^\mp$. We cannot extract branching fractions for $K^{*0}\overline{K}^{*0}$ or $K^*(892)^+ K^*(892)^-$, but our results for $K^*(892)^+ K^- \pi^0 + c.c.$ and $K^*(892)^\pm K_S^0 \pi^\mp$ are both consistent with the world-average value for $K^*(892)^+ K^*(892)^-$, indicating the same dominance of $K^*(892)^+ K^*(892)^-$ as in non-J/ψ data. Our results for $K^{*0} K^+ \pi^- + c.c.$ and $K^{*0} K_S^0 \pi^0 + c.c.$ respectively are about five and two times larger than

the world-average value for $K^{*0}\overline{K}^{*0}$.

[1] M. Davier, S. Eidelman, A. Höcker; Z. Zhang, Eur. Phys. J. C **31**, 503 (2003); M. Davier, A. Hoecker, B. Malaescu, and Z. Zhang, Eur. Phys. J. C **71**, 1515 (2011); K. Hagiwara et al., J. Phys. G **38**, 085003 (2011).

[2] V. N. Baier and V. S. Fadin, Phys. Lett. B **27**, 223 (1968).

[3] A. B. Arbuzov et al., J. High Energy Phys. **12**, 009 (1998).

[4] S. Binner, J.H. Küehn and K. Melnikov, Phys. Lett. B **459**, 279 (1999).

[5] M. Benayoun et al., Mod. Phys. Lett. A **14**, 2605 (1999).

[6] H. Czyz, A. Grzelinska, J. H. Kühn and G. Rodrigo, Eur. Phys. J. C **33**, 333 (2004).

[7] J. P. Lees et al. (BABAR Collaboration), Phys.Rev. D **88**, 032013 (2013);
J. P. Lees et al. (BABAR Collaboration), Phys.Rev. D **92**, 072008 (2015).

[8] J. P. Lees et al., (BABAR Collaboration), Phys.Rev. D **86**, 012008 (2012).

[9] J. P. Lees et al. (BABAR Collaboration), Phys. Rev. D **89**, 092002 (2014).

[10] B. Aubert *et al.* (*BABAR* Collaboration), Phys. Rev. D **77**, 092002 (2008).

[11] J. P. Lees *et al. BABAR* Collaboration, arXiv:1701.08297 (2017), Accepted by Phys. Rev. D.

[12] B. Aubert *et al.* (*BABAR* Collaboration), Nucl. Instrum. and Meth. A **479**, 1 (2002); B. Aubert *et al.* (*BABAR* Collaboration), Nucl. Instrum. and Meth. A **729**, 615 (2013).

[13] J. P. Lees *et al.* (*BABAR* Collaboration), Nucl. Instr. and Meth. A **726**, 203 (2013).

[14] H. Czyz and J. H. Kühn, Eur. Phys. J. C **18**, 497 (2001); H. Czyz, A. Grzelinska, J. H. Kühn and G. Rodrigo, Eur. Phys. J. C **47** 617 (2006).

[15] A. B. Arbuzov *et al.*, J. High Energy Phys. **10**, 001 (1997).

[16] M. Caffo, H. Czyz, E. Remiddi, Nuovo Cim. Soc. Ital. Fis. A **110**, 515 (1997); Phys. Lett. B **327**, 369 (1994).

[17] E. Barberio, B. van Eijk, and Z. Was, Comput. Phys. Commun. **66**, 115 (1991).

[18] T. Sjöstrand, Comput. Phys. Commun. **82**, 74 (1994).

[19] S. Jadach and Z. Was, Comput. Phys. Commun. **85**, 453 (1995).

[20] S. Agostinelli *et al.* (GEANT4 Collaboration), Nucl. Instrum. Methods Phys. Res., Sect. A **506**, 250 (2003).

[21] Review of Particle Physics, K.A. Olive *et al.*, Chin. Phys. C **38**, 090001 (2014).

[22] B. Aubert *et al.* (*BABAR* Collaboration), Phys. Rev. D **70**, 072004 (2004).

[23] B. Aubert *et al.* (*BABAR* Collaboration), Phys. Rev. D **73**, 052003 (2006).

[24] G.J. Gounaris and J.J. Sakurai, Phys. Rev. Lett. **21** 244 (1968).